ISSN 0252-1075
Contribution from IITM
Technical Report No. 13
ESSO/IITM/ART/TR/04(2026)/210

Atmospheric Radiation Observatory at Atmospheric Research Testbed (ART) facility in the Indian Monsoon Core Zone for Climate Studies

**B. Padmakumari, Udaya Kumar Sahoo, Jeni Victor, Yang Lian,
Anil Kumar Sahu, V. Anil Kumar, T. R. Libin, G. Pandithurai**

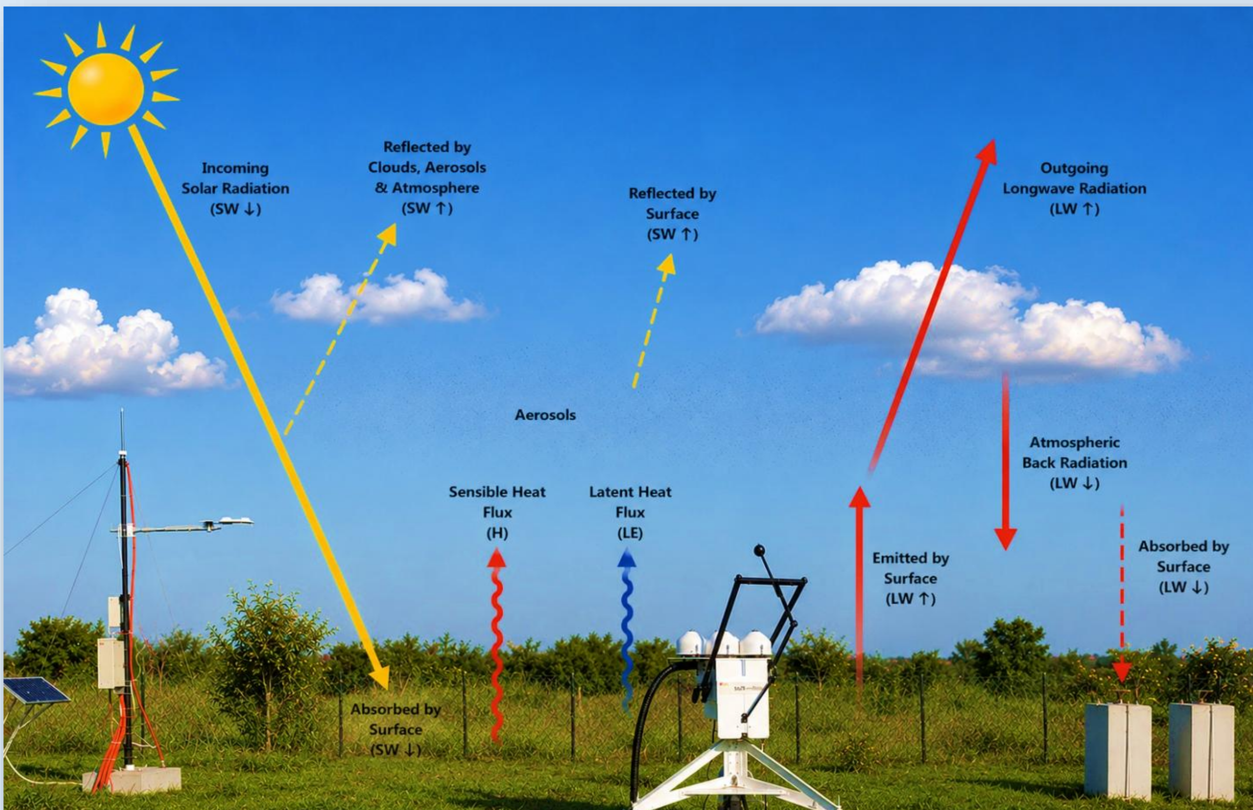

Atmospheric Research Testbeds (ART)
Indian Institute of Tropical Meteorology (IITM)
Ministry of Earth Sciences (MoES)
Pune, India
http://www.tropmet.res.in/

ISSN 0252-1075
Contribution from IITM
Technical Report No. 13
ESSO/IITM/ART/TR/04(2026)/210

Atmospheric Radiation Observatory at Atmospheric Research Testbed (ART) facility in the Indian Monsoon Core Zone for Climate Studies

B. Padmakumari*, Udaya Kumar Sahoo, Jeni Victor, Yang Lian,
Anil Kumar Sahu, V Anil Kumar, T. R Libin & G. Pandithurai

***Corresponding Author**

Dr. B. Padmakumari
Scientist F & Project Director
Atmospheric Research Testbeds (ART)
Indian Institute of Tropical Meteorology,
Dr. Homi Bhabha Road, Pashan,
Pune-411 008, Maharashtra, India.
E-mail: padma@tropmet.res.in

Atmospheric Research Testbeds (ART)
Dr. B. Padma Kumari
Project Director

Indian Institute of Tropical Meteorology (IITM)
Ministry of Earth Sciences (MoES), Government of India
Dr. Homi Bhabha Road, Pashan, Pune – 411008, India
http://www.tropmet.res.in/

DOCUMENT CONTROL SHEET

Ministry of Earth Sciences (MoES)

Indian Institute of Tropical Meteorology (IITM)

ESSO Document Number

ESSO/IITM/ART/TR/04(2026)/210

Title of the Report

Atmospheric Radiation Observatory at Atmospheric Research Testbed (ART) facility in the Indian Monsoon Core Zone for Climate Studies

Authors

B. Padmakumari, Udaya Kumar Sahoo, Jeni Victor, Yang Lian, Anil Kumar Sahu, V Anil Kumar, T. R Libin, G. Pandithurai

Type of Document

Technical Report

Number of pages and figures

49, 18

Keywords

Solar radiation, terrestrial radiation, net radiation, radiation budget, monsoon core zone, instrument calibration and QC, remote monitoring, supersite

Security classification

Open

Distribution

Unrestricted

Date of Publication

July 2026

Table of Contents

List of Figures

Abstract

The Atmospheric Radiation Observatory (ARO) has been established at the Atmospheric Research Testbed (ART) facility in the monsoon core zone (MCZ) of Central India near Bhopal, Madhya Pradesh, for measurements of surface radiation and related atmospheric parameters. The observatory is equipped with state-of-the-art radiometric instrumentation for measuring the components of surface radiation budget, including global, diffuse, and direct solar irradiance, longwave radiation, net radiation, photosynthetically active radiation (PAR), ultraviolet (UV) radiation, and sunshine duration. A precision sun tracker, integrated ventilation systems, and an indigenously developed real-time data acquisition, visualization, and archival system ensure reliable operation, continuous monitoring, and long-term data management.

The observatory follows standard operating procedures for instrument operation, maintenance, calibration, and quality assurance in accordance with the recommendations of the World Meteorological Organization (WMO). This report documents the radiometric instrumentation, observational methodology, calibration procedure, quality-control framework, and post-processing protocols implemented to ensure the generation of high-quality radiation datasets. Representative analyses of the diurnal and seasonal variability of key radiation parameters under different sky conditions demonstrate the pronounced variability in surface radiation over the MCZ, reflecting the influence of changing atmospheric and cloud conditions.

The observations from ARO constitute a valuable resource for studies of the Earth's surface radiation budget, aerosol–cloud–radiation interactions, monsoon processes, climate variability, and renewable energy applications over Central India. The facility is envisioned as a supersite for the intercomparison and validation of ground-based and satellite-derived radiation products, as well as for the evaluation and improvement of weather and climate models.

Executive Summary

The ARO has been established at ART facility in the MCZ of Central India for continuous measurements of surface radiation and associated atmospheric parameters. The observatory is equipped with a comprehensive suite of high-precision radiometric instruments, including pyranometers, pyrheliometers, pyrgeometers, ultraviolet sensors, a photosynthetically active radiation sensor, a net radiometer, and a sunshine duration recorder. A precision sun tracker, integrated ventilation systems, and an indigenously developed real-time data acquisition, visualization, and archival system enable continuous observations, operational reliability, and long-term data management. The observatory follows internationally accepted operational and maintenance practices recommended by WMO.

This report documents the instrumentation, observational methodology, calibration procedure, data acquisition system, quality-control framework, and post-processing techniques adopted at ARO. Data quality is maintained through comprehensive quality-control procedures, including physical consistency tests, temporal continuity analysis, clear-sky model evaluation, statistical outlier detection, and routine calibration and intercomparison with reference radiometers. Missing observations are addressed using a hierarchy of gap-filling approaches, including interpolation for short-duration gaps, model-assisted reconstruction using ancillary meteorological observations, and machine learning-based imputation for longer data gaps and periods characterized by highly variable atmospheric conditions. Regular intercomparison with reference radiometers ensured measurement reliability and long-term stability of the observational record.

Analysis of radiation measurements demonstrates the sensitivity of surface radiation fluxes to cloud cover, aerosol loading, and atmospheric moisture over the MCZ of Central India. Under clear-sky conditions, direct solar radiation dominates the incoming shortwave flux, resulting in high global horizontal irradiance, enhanced PAR and UV radiation, and comparatively lower downward longwave radiation due to the relatively dry atmosphere. In contrast, cloudy and overcast conditions substantially suppress direct solar radiation, increase the diffuse radiation component through multiple scattering, and enhance downward longwave radiation because of increased atmospheric emissivity associated with clouds and moisture.

Seasonal analysis further reveals the imprint of monsoon dynamics on the regional radiation budget. Surface shortwave radiation reaches its maximum during the pre-monsoon season (~900

Wm^{-2}) under relatively cloud free conditions and high solar elevation, decreases significantly during the monsoon (~500 Wm^{-2}) due to persistent cloud cover and enhanced attenuation. Partially recovers during the post-monsoon (~700 Wm^{-2}) as skies clear following monsoon withdrawal and remains comparatively lower during winter (~600 Wm^{-2}) owing to reduced solar elevation, shorter day length, and attenuation from fog and haze.

The datasets generated by ARO constitute a valuable resource for studies of the Earth's surface radiation budget, aerosol–cloud–radiation interactions, monsoon dynamics, climate variability, and renewable energy assessment. The observatory is envisioned as a supersite for the intercomparison and validation of ground-based and satellite products, as well as for the evaluation and improvement of numerical weather prediction and climate models. Through sustained quality observations and adherence to international measurement standards, this facility could significantly support national and international research programs focused on weather, climate, and environmental monitoring and build collaborations. Continued operation and periodic calibration are recommended to maximize scientific and societal benefits.

1. Introduction:

Solar radiation (SR) is the fundamental driver of the Earth's climate system, playing a critical role in atmospheric circulation, the hydrological cycle and biospheric productivity (Wild, 2012). Accurate measurements of its components including global, diffused and direct shortwave radiation, longwave terrestrial and net radiation are essential for understanding surface energy balance, seasonal variability, and long-term climate trends (Augustine et al., 2000; Driemel et al., 2018). In central India, particularly within the monsoon core zone, solar insolation varies considerably due to the complex interplay of cloud dynamics, aerosol loading, humidity, and monsoonal influences (Kazadzis et al., 2018).

The SR measurements provide a direct estimate of the rate at which radiant energy reaches the Earth's surface of a known area. Radiative energy can be expressed as radiant flux (energy received, emitted, or transmitted per unit time), radiance (radiation falling within a given solid angle), radiant flux density (radiative flux per unit area), irradiance (radiant flux density incident on a surface) and emittance (radiant flux density emitted from a surface). These quantities are generally expressed in watts per meter square (Wm^{-2}).

The spectral distribution of radiation emitted by a body is governed by its temperature according to Planck's law (defined as the wavelength of maximum emission by a blackbody is inversely proportional to its absolute temperature). Consequently, the sun (~6000 K) radiates most of its energy at shorter wavelengths, while the cooler earth (288 K) primarily emits radiation at longer wavelengths. Based on this distinction, the natural radiation field at the earth's surface is conventionally divided into two distinct broadband spectral regions, the 'shortwave' (solar) radiation (approximate wavelength range: 0.3 to 3 μm) and 'longwave' (terrestrial) radiation (wavelength range: 3 to 100 μm).

At the top of the atmosphere, the mean incoming solar radiation is ~ 1367 Wm^{-2} (± 3 %, resulting from changes in the Earth's orbital distance from the Sun). However, only a fraction of this radiation reaches the Earth's surface as it undergoes complex multiple scattering, absorption and emission processes by aerosols, atmospheric gases, clouds and water vapour (Padma Kumari et al., 2007, 2010; Long and Shi, 2008; Wild, 2012; Kazadzis et al., 2018). These atmospheric constituents also regulate the emission and absorption of terrestrial longwave radiation, thereby controlling the surface radiation balance.

Long-term high-quality measurements of surface radiation are essential for assessing the Earth's radiation budget, monitoring climate variability, and improving weather and climate predictions. Variations in aerosols, clouds, water vapour and greenhouse gases substantially influence both incoming solar and outgoing terrestrial radiation, making long-term, high-quality radiation observations indispensable for climate research. Such measurements also provide critical information for evaluating climate models, satellite-derived radiation products, and land-atmosphere interactions.

Hence, continuous observations are very much essential especially in Central India (CI), which mainly comprises of the monsoon core zone (MCZ), a region characterized by strong land-atmosphere coupling and intense monsoon convection that significantly influences the regional hydrological cycle and global climate system. Despite its climatic importance, long-term, comprehensive surface radiation measurements over this region remain limited. To address this observational gap and facilitate integrated atmospheric research, the Atmospheric Research Testbed (ART) has been established in Central India, similar to the international Atmospheric Radiation Measurement (ARM) observatories in the United States (Augustine et al., 2000; Haeffelin et al., 2012; Driemel et al., 2018). By combining continuous radiation, aerosol, cloud, and meteorological observations, ART provides a unique platform for advancing the understanding of monsoon processes, aerosol–cloud–radiation interactions, and climate variability over one of the most climatically sensitive regions of the Indian subcontinent.

The ARO established at the ART facility is equipped with state-of-the-art, high-precision radiometric instruments for continuous measurements of surface radiation parameters. The observatory provides high-quality, long-term datasets that are essential for quantifying the Earth's energy budget, understanding aerosol–cloud–radiation interactions and climate feedback, and evaluating satellite products, radiation monitoring networks, and numerical weather and climate models. Through rigorous calibration and quality-control procedures, the observations are maintained at standards making the facility a valuable resource for advancing atmospheric, climate, and renewable energy research (Driemel et al., 2018; Gröbner et al., 2014; Sengupta et al., 2015; Younes et al., 2017).

2. Scope of the Report:

This report presents a comprehensive overview of the ARO. It describes the observatory, deployment strategy, and integrated radiometric measurement systems, together with the real-time data acquisition and monitoring framework developed for continuous, high-resolution observations of solar and terrestrial radiation. The report also outlines the initial quality-control procedures, calibration practices, and data validation methodologies implemented to ensure the accuracy, reliability, and long-term consistency of the observational record.

The report further presents the observational characteristics and variability of key radiative parameters, including shortwave, longwave, ultraviolet, photosynthetically active radiation, and sunshine duration under different atmospheric conditions. Emphasis is given to the temporal variability of surface radiative fluxes and their response to changing meteorological conditions, providing insight into the surface radiation budget and radiative energy exchange processes over Central India.

In addition, the report highlights the scientific relevance and potential applications of the datasets for studies of the Earth's radiation budget, surface energy balance, aerosol–cloud–radiation interactions, satellite product evaluation, renewable energy resource assessment, and the evaluation and improvement of numerical weather prediction and climate models particularly over the Indian monsoon region**.**

3. Relevance of the facility:

The ART facility is strategically located in the MCZ of Central India, in close proximity to the Tropic of Cancer, making it an important observational site for studying tropical radiative and monsoon-driven atmospheric processes. The region experiences intense solar heating during the pre-monsoon season under clear-sky conditions, while monsoon periods are characterized by deep convection, enhanced cloud cover, and strong attenuation of incoming solar radiation (Gadgil, 2003; Padma Kumari and Goswami, 2010; Wild, 2012; Kazadzis et al., 2018).

The site is influenced by several synoptic and regional scale atmospheric systems, including southwest monsoon flow, pre-monsoon heat-low circulation, monsoon depressions originating from the Bay of Bengal, and occasional western disturbances during winter. The prevailing winds exhibit seasonal transition from dry north-westerly and westerly continental air masses in the pre-monsoon months to moist south-westerly monsoonal winds during the rainy season (Gadgil, 2003). The observatory is also favourably positioned between the Indo-Gangetic Plain (IGP) and the Thar Desert, enabling observation of aerosol transport associated with dust intrusion, biomass burning, anthropogenic pollution, and long-range aerosol advection (Moorthy et al., 2007; Lau et al., 2006). This transitional semi-arid to sub-humid climatic environment, relatively homogeneous terrain, and minimal urban obstruction make the site highly suitable for investigating cloud–aerosol–radiation interactions, surface energy exchange, and monsoon-related radiative processes under tropical continental conditions (Younes et al., 2017). The observations also provide regionally representative datasets for satellite product validation, radiative transfer studies, and improvement of NWP and climate model simulations over Central India (Sengupta et al., 2015; Driemel et al., 2018).

The India Meteorological Department (IMD) presently operates a network of 47 solar radiation stations across diverse climatic regions of India for routine measurements of shortwave and longwave radiation components, supplemented by conventional sunshine duration observations. ARO has been conceived as a supersite for comprehensive observations of all the components of the Earth's radiation budget and associated atmospheric processes over Central India. Its integrated suite of high-precision radiometric and other atmospheric and meteorological instrumentation enables continuous and simultaneous measurements of multiple radiation components, thereby providing an advanced observational platform for atmospheric radiation research, satellite product validation, and renewable energy assessment.

4. Site Description:

The ART facility is established in Silkheda, Sehore district of Madhya Pradesh in India. Geographically, the site lies at 23.57°N, 77.24°E, with an elevation of 471 meters above mean sea level (Figure 1). It is situated approximately 40 kilometers northwest of Bhopal, the capital of Madhya Pradesh. The ART facility is strategically located in the heart of the monsoon core zone of central India, a region known for its high seasonal variability in solar radiation, precipitation, and atmospheric dynamics. The surrounding terrain is characterized by a mix of semi-arid to sub-humid conditions, interspersed with agricultural fields and sparse vegetation, making it an ideal natural observatory for measurements of different components of atmospheric and solar radiation under diverse climatic influences.

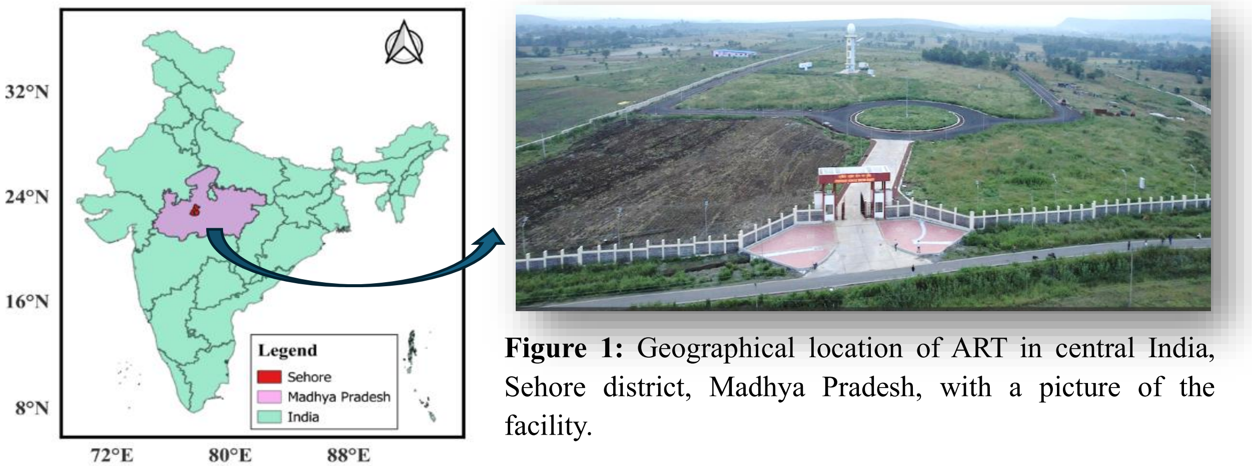

Figure 1: Geographical location of ART in central India, Sehore district, Madhya Pradesh, with a picture of the facility.

5. Instrumentation & Layout plan:

The ARO is established in an open observational field, designed to provide an unobstructed hemispheric sky view and minimal environmental interference for accurate radiative flux measurements, as illustrated in Figure 2.

The instrumentation deployed at the observatory includes:

1. **Pyranometer** – Measures global horizontal irradiance (GHI) representing the total shortwave (SW) radiation incident on a horizontal surface.
2. **Shaded Pyranometer** – Measures diffused horizontal irradiance (DHI) by blocking the direct solar beam using a shading mechanism, thereby capturing the diffuse component of SW radiation.
3. **Pyrheliometer** – Measures direct normal irradiance (DNI) representing the direct beam component of solar radiation.
4. **Pyrgeometer** – Measures longwave (LW) radiation emitted by the atmosphere, important for surface energy exchange studies.
5. **Net Radiometer** – Simultaneously measures incoming and outgoing SW and LW radiation components for estimating net radiation and surface energy balance.
6. **PAR Sensor** – Measures photosynthetically active radiation within the spectral range important for vegetation and ecosystem studies.

7. **UV Radiometers** – Monitor UV-A, UV-B, and UV-E radiation components for atmospheric, environmental, and UV exposure studies.
8. **Sunshine Duration Recorder** – Measures effective sunshine duration based on DNI thresholds, supporting clear-sky and cloud variability analysis.
9. **Sun Tracker** – A dual-axis solar tracking system for continuous and precise alignment of radiometric instruments with the solar disk, throughout the day.
10. **Ventilation Units** – Integrated with radiometric sensors to minimize condensation, dust accumulation, and environmental effects, thereby ensuring stable long-term observations and measurement accuracy.

The key technical specifications of the above instrumentation are summarized in **Table 1 (Annexure-I)**. More detailed technical description of each sensor is provided in **Annexure II**

Figure 2: Atmospheric Radiation Observatory (ARO) facility layout, featuring instruments for measuring the components of atmospheric radiation.

The instrumentation layout has been designed in accordance with the guidelines of the WMO observational practices, ensuring optimal sensor exposure, appropriate spatial distribution, and minimal interference from mutual and surrounding shadings. As shown in Figure 2, a SOLYS2 sun tracker is centrally deployed to support pyranometer, pyrheliometer and pyrgeometer. The tracker position ensures precise solar alignment and symmetrical sky exposure throughout the year.

A dedicated platform has been established for UV radiation monitoring sensors, while a separate platform is provided to carry out periodic intercomparison and calibration of the radiation sensors. Net Radiometer (CNR4), PAR and sunshine recorder (CSD-3) are mounted on individual masts positioned at appropriate distances. The overall site configuration is optimized to facilitate continuous and high-quality observations of atmospheric radiation and surface energy exchange processes under diverse atmospheric conditions.

5.1 SW & LW Monitoring Systems:

The SW and LW radiation measurement systems are integrated on a high-precision SOLYS2 dual-axis sun tracker designed for continuous and accurate alignment with the solar disk throughout the diurnal cycle. The tracker enables real-time solar tracking, ensuring precise sensor orientation with the Sun's apparent motion and minimizing angular alignment errors. The platform supports simultaneous observations of GHI, DHI, DNI, and atmospheric LW radiation. The suite of instrumentation comprises an unshaded pyranometer for GHI, a shaded pyranometer equipped with an automated shadowing mechanism for DHI, a pyrheliometer for DNI, and a pyrgeometer for monitoring atmospheric LW radiation fluxes. The coordinated operation of these instruments on a dynamically oriented platform ensures high-quality and internally consistent radiation measurements for atmospheric and surface energy balance studies.

The SOLYS2 system (Kipp & Zonen, 2018a) is equipped with an integrated GNSS receiver for automatic geolocation and time synchronization, eliminating the need for external computing interfaces. The tracker features a rugged cast aluminium enclosure with flexible mounting capability, enabling stable operation under extreme environmental conditions ranging from –40 °C to +50 °C. The platform supports concurrent operation of multiple precision radiometers, making it suitable for long-term atmospheric radiation monitoring and climate research applications.

As illustrated in Figure 3, the sun tracker is mounted on a reinforced concrete tripod platform elevated approximately 1 m above ground level to minimize surface-induced thermal effects and mechanical vibrations. In addition, the integrated sun sensor enables active solar tracking, thereby improving pointing accuracy during transient cloud conditions.

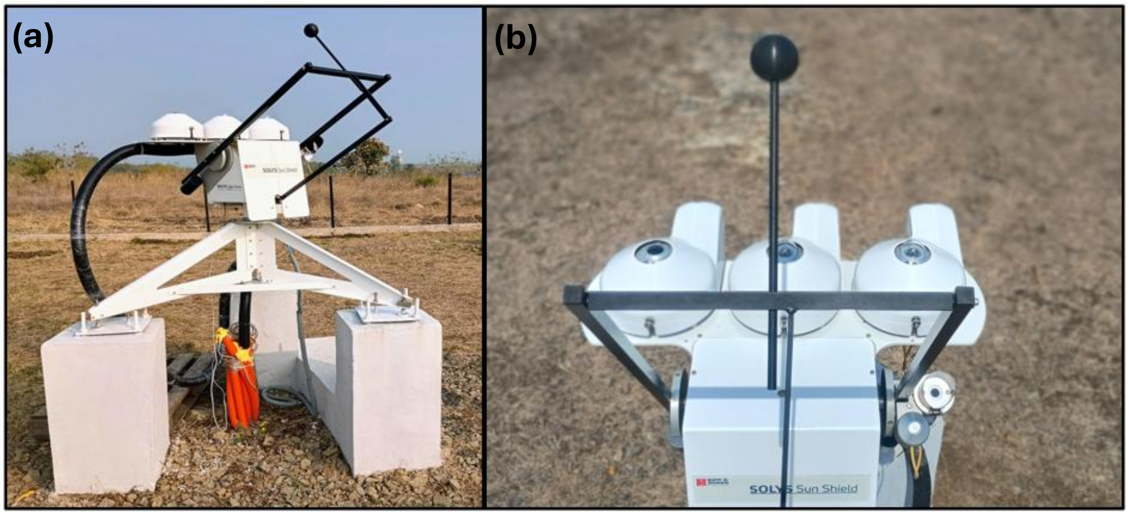

Figure 3: (a) Sun Tracker with a shading mechanism; (b) radiometers mounted on a sun tracker for precise irradiance measurements.

5.2 UV Radiation Monitoring System:

The UV radiation monitoring system consists of high-precision UV-A, UV-B, and UV-E radiometers installed on a dedicated measurement platform for continuous monitoring of ultraviolet radiation components. As shown in Figure 4, the sensors are mounted on individual reinforced concrete pedestals elevated approximately 1 m above ground level to ensure unobstructed exposure, minimize ground-induced effects, and maintain measurement stability under adverse environmental conditions.

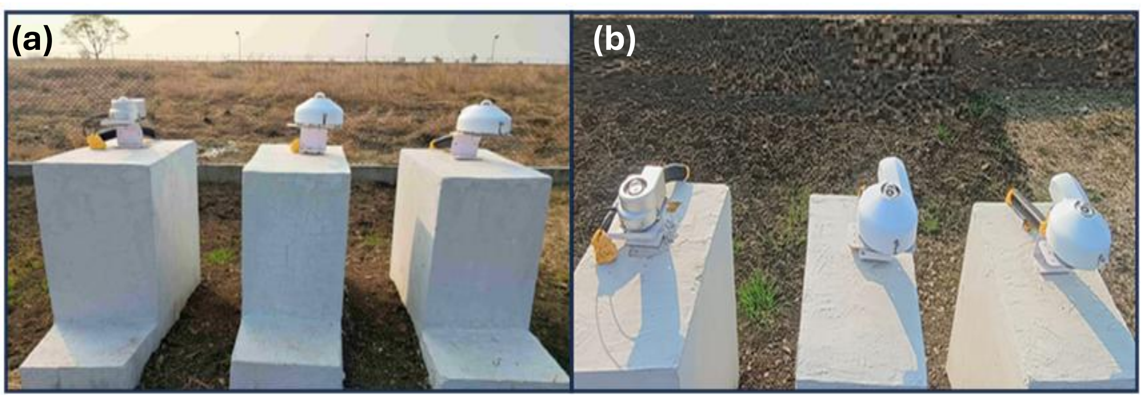

Figure 4: UV radiation monitoring systems. (a) Front view and (b) top view of UV sensors, showing UV-A, UV-B, and UV-E (from left to right).

The UV-A and UV-B radiometers provide continuous measurements of surface UV irradiance, supporting studies of atmospheric composition, ozone variability, photochemical processes, and radiative forcing. The UV-E radiometer extends the observations to shorter UV wavelengths, enabling investigations of high-energy solar radiation interactions with the upper atmosphere and ionosphere.

5.3 Net Radiometer:

The net radiometer (CNR4) is installed on a dedicated mast-mounted platform at a height of approx. 2 m above the ground level for continuous measurements of surface radiation budget related components. The sensor is mounted with a horizontal offset from the mast structure to minimize self-shading and ground-induced radiative interference, thereby ensuring accurate radiative flux measurements. As shown in Figure 5, the instrument incorporates four precision radiometric sensors for simultaneous measurements of upwelling (UW) and downwelling (DW) SW and LW radiation components. The four-component configuration enables real-time determination of net radiation and surface albedo, both of which are critical parameters for surface energy balance studies. The data obtained from the CNR4 sensor are fundamental for quantifying surface heat exchange, latent and sensible heat fluxes, and evapotranspiration rates. Moreover, these measurements contribute significantly to understanding the influence of different land surface types, such as vegetation, bare soil, or water bodies, on local and regional energy budgets.

Figure 5: Net Radiometer mounted on a mast for measuring both upwelling and downwelling SW and LW radiations

5.4 PAR sensor and Sunshine Duration Recorder:

A dedicated mast-mounted observational platform supports the installation of the CSD3 Sunshine Duration sensor and the PAR sensor at a height of approximately 2 m above ground level. As shown in Figure 6, the CSD3 is installed with a north–south orientation and a tilt angle of 23.5°, following the manufacturer recommended installation practices to ensure optimal exposure to direct solar radiation throughout the year. The CSD3 continuously measures effective sunshine duration by identifying periods when direct solar irradiance exceeds the threshold of 120 W m^{-2}. Sunshine duration is estimated from the cumulative duration of irradiance values exceeding this threshold and is widely used in climate monitoring, solar energy assessment, and cloud variability studies.

The PAR sensor continuously measures photosynthetically active radiation within the spectral range relevant to plant physiological activity and ecosystem productivity. The deployment of the PAR sensor and CSD3 enables continuous monitoring of both biologically relevant and energetically significant solar radiation parameters under diverse atmospheric conditions.

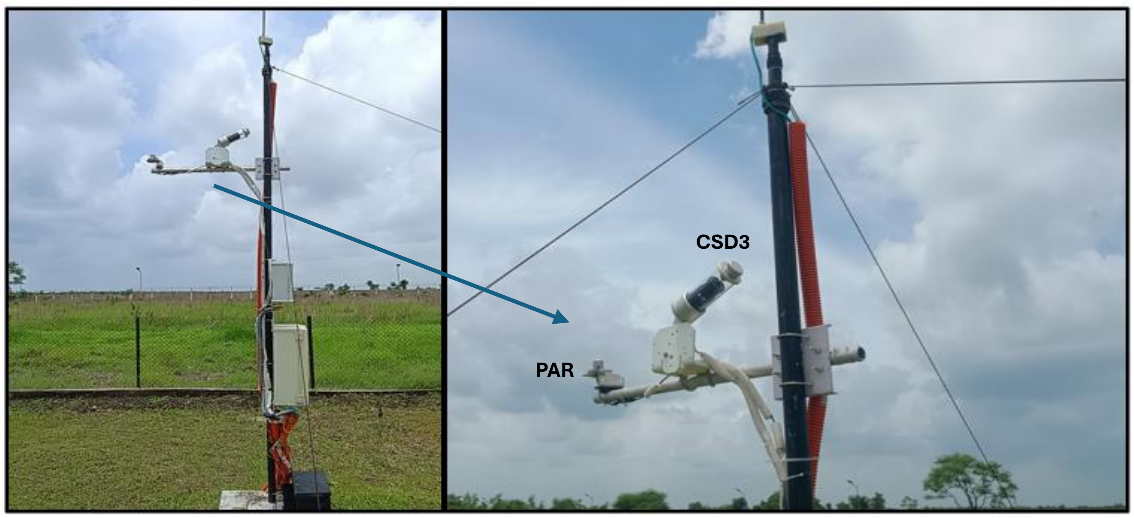

Figure 6: Mounting arrangements of sunshine duration (CSD3) and PAR sensors

Each mast is integrated with a self-contained instrumentation enclosure housing programmable dataloggers, GPS receivers, AC/DC power supply systems, auxiliary solar power units, Modbus communication converters, and structured cable management systems. This integrated configuration ensures reliable data acquisition, storage, and remote transmission of observational datasets. To ensure operational safety and long-term reliability under adverse weather conditions, both mast systems are equipped with lightning arresters and dedicated chemical earthing systems for protection against electrical surges and lightning-induced damage. These protective measures support uninterrupted operation and long-term observational continuity of the radiation monitoring systems.

5.5 Ventilation Unit:

Each radiometric sensor is equipped with an automatic ventilation unit (CVF4) designed to prevent condensation and dust accumulation on the optical domes. By maintaining clean and dry sensor surfaces, this unit helps to preserve measurement accuracy and ensure the long-term stability of radiometric observations. The ventilation systems support continuous operation under varying environmental conditions and contribute to improved data quality by reducing maintenance requirements and minimizing measurement uncertainties.

5.6 Inter-comparison & Validation Platform:

The observatory also includes dedicated platforms for periodic intercomparisons, validation, and calibration of radiometric instruments. These platforms provide a stable observational setup for evaluating sensor performance, maintaining measurement consistency, and ensuring long-term reliability of radiation observations. Regular traceable calibration and intercomparison exercises are essential for minimizing sensor drift, compensating for environmental influences, and reducing performance degradation associated with prolonged field exposure. These procedures support the generation of accurate, stable, and scientifically reliable radiation datasets suitable for long-term climatological and radiative transfer studies.

6. Data Access and Visualization:

The observatory employs two Aeron XTREME data loggers for continuous high-resolution acquisition of radiometric observations from the integrated sensor network. The data loggers are designed for research-grade atmospheric measurements and incorporate a 24-bit analog-to-digital converter (ADC) with >20 Effective Number of Bits (ENOB), enabling high-precision acquisition of low-amplitude radiometric signals. The system supports sensor sampling rates up to 200 Hz, facilitating stable high-frequency measurements required for advanced atmospheric radiation studies and long-term observational applications. Detailed technical specifications of the data logging system are provided in **Annexure II.**

To support continuous monitoring and efficient management of observational datasets, the facility incorporates a multi-tiered data access and visualization framework consisting of on-site monitoring interfaces, remote data access systems, and a custom-developed real-time visualization platform. These integrated systems enable real-time observation, storage, retrieval, and visualization of radiation parameters for operational monitoring and scientific analysis.

6.1 On-Site Display:

The first level of data monitoring is facilitated by a dedicated field display unit directly integrated with the data logger. This on-site alphanumeric display provides immediate access to live sensor readings in real time, allowing field personnel to perform rapid system checks and verify sensor functionality during maintenance or deployment.

6.2 Remote Monitoring:

To enable remote and centralized system management, the data loggers are connected to a high-performance computer system located in the control room using Ethernet-based communication. Through this network, users can access a proprietary data monitoring application designed for remote observation and configuration of the data logging system. The application provides secure remote access through a dedicated IP address, requiring user authentication via a login window, as shown in Figure 7. This security feature ensures that only authorized personnel can interact with the system, thereby maintaining data integrity and preventing unauthorized modifications. Upon successful login, users can perform a range of critical functions, including, historical data retrieval for offline analysis and configuration adjustments such as modifying sensor parameters, data logging intervals, or communication settings.

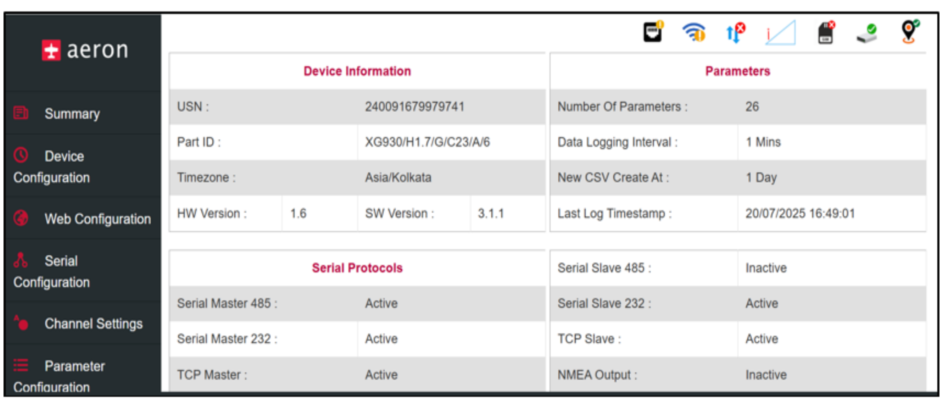

Figure 7: Data visualization interface.

6.3 In-house Developed Real-Time Data Visualization Application:

To enhance the observatory's operational and analytical capabilities, an in-house real-time data visualization application was developed for continuous acquisition, visualization, and storage of high-frequency radiation measurements. The software integrates real-time plotting, automated data logging, and a user-friendly interface, providing an efficient platform for instrument monitoring and quality control.

The application communicates with the Aeron data logger using the MODBUS over TCP/IP protocol (Zagan and Gaitan, 2022) through a local Ethernet network. A dedicated communication thread continuously acquires measurements from the connected sensors without interrupting the visualization process. The acquired observations are displayed in real time, enabling continuous monitoring of instrument performance and rapid identification of communication failures or anomalous sensor behavior.

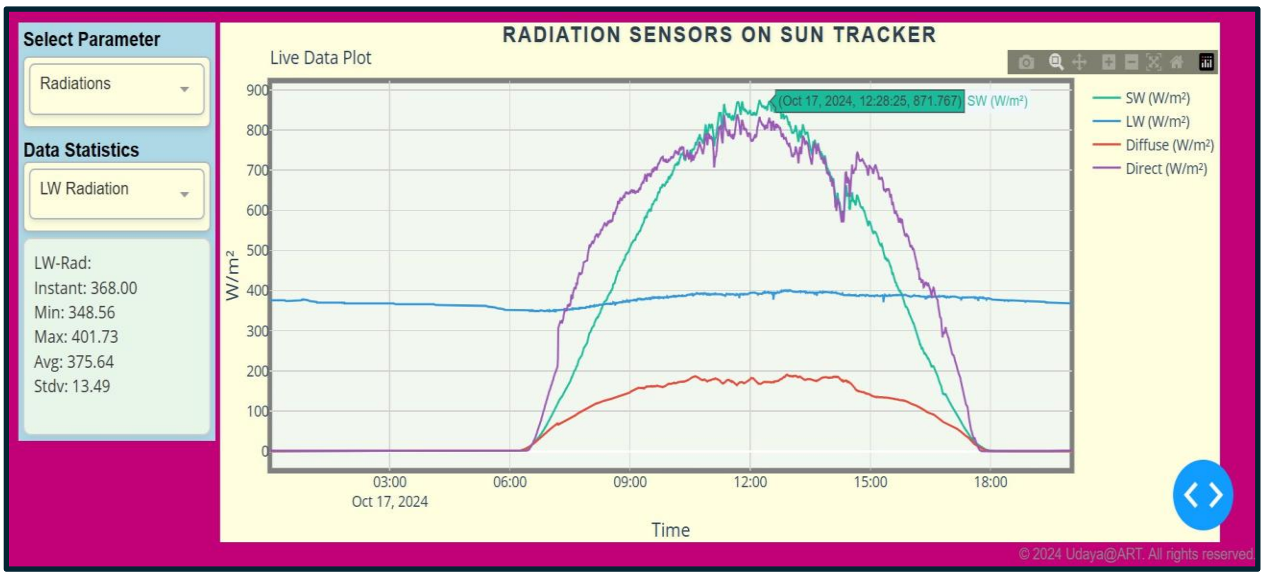

Figure 8: Real-time data acquisition and visualization interface.

To ensure reliable long-term data archival, the application incorporates an automated logging module that stores observations in structured CSV files at a default temporal resolution of 60 s. The files are automatically named using timestamp-based conventions and organized into date-wise directories, facilitating efficient data management, retrieval, and archival. The CSV format provides compatibility with widely used scientific data analysis platforms, including MATLAB, Python, R, and Microsoft Excel, thereby enabling seamless integration into subsequent processing and analysis workflows. Figure 8 presents the graphical user interface of the application, illustrating the real-time visualization of incoming observations together with the automated data logging capability that supports continuous monitoring of the solar radiation measurement system.

7. Data Quality Control and Assurance

To ensure the accuracy, reliability, and continuity of the measurements, all observations from the ARO undergo systematic quality-control and validation procedures. The quality assurance framework integrates automated screening, temporal consistency analysis, clear-sky model validation, redundancy verification, and advanced gap-filling techniques to maintain high-quality long-term radiation datasets.

7.1 Initial data screening:

The raw observations undergo an automated pre-processing procedure to identify missing values, sensor malfunctions, and physically unrealistic measurements before archival and analysis. The initial screening process includes multiple quality-control checks to ensure the consistency and integrity of the observational datasets. These checks include:

7.1.1 Flagging of Missing or Corrupted Records:

Records containing null values, invalid entries, communication gaps, or incorrect timestamps were identified and flagged to prevent the propagation of erroneous data into subsequent analyses. A binary quality flag was assigned to each observation as

$$F(i) = \begin{cases} 1, & \text{if } R(i) \text{ is missing, corrupted, or invalid} \\ 0, & \text{otherwise} \end{cases}$$

where $F(i)$ is the quality flag for the i^{th} record and $R(i)$ is the corresponding observation. Flagged records were excluded from further processing or subjected to additional quality control checks.

7.1.2 Range Checks:

Radiation measurements were subjected to physical range checks to ensure the quality of the data. For shortwave radiation, GHI, DHI, and DNI were examined using physically realistic limits based on solar geometry and extraterrestrial solar irradiance. The fundamental radiative closure relationship as bellow.

$$\text{GHI} = \text{DHI} + \text{DNI} \times \cos(\theta z),$$

where θz is the solar zenith angle, was used as an additional consistency check. Typical operational ranges adopted for quality control were 0–1400 Wm^{-2} for GHI, 0–800 Wm^{-2} for DHI, 0–1200 Wm^{-2} for DNI, 150–700 $W\ m^{-2}$ for longwave radiation, 0–90 Wm^{-2} for UV-A, 0–9 Wm^{-2} for UV-B, 0–1W m^{-2} for UV-E, 0–3000 μmol $m^{-2}\ s^{-1}$ for PAR, 0–1 for surface albedo, and 0–60 $minh^{-1}$ for sunshine duration. These limits were supplemented by checks for physically plausible daytime and nighttime behaviour and were evaluated considering the climatological characteristics of the

Central India monsoon region to ensure the generation of reliable and high-quality radiation datasets.

7.1.3 Rate-of-Change Checks:

Rate-of-change checks are used to detect abrupt and unrealistic temporal variations in radiation measurements that may result from sensor malfunctions, communication and data logging errors, electronic noise, transient spikes, or other measurement anomalies. By identifying and flagging such observations, the procedure improves the temporal consistency and overall quality of the radiation dataset. Successive observations were examined using the first-order difference as bellow.

$$\Delta R = R(t) - R(t-1)$$

where R(t) and R (t − 1) represent the radiation measurements at the current and previous time steps, respectively. The rate of change was estimated as

$$\frac{dR}{dt} = \frac{R(t) - R(t-1)}{\Delta t}$$

where Δt is the sampling interval. Observations exhibiting anomalously large temporal variations were flagged for further quality assessment.

7.2 Statistical and visual outlier detection:

Statistical outlier detection techniques, including boxplot analysis and Z-score evaluation, were applied to the SW and LW radiation datasets to identify abnormal observations and extreme deviations from expected measurement behaviour. These analyses assist in distinguishing genuine atmospheric variability, such as changes associated with cloud cover and transient weather conditions, from non-atmospheric anomalies arising from sensor malfunctions, communication errors, maintenance activities, or other operational issues. The results of the statistical screening are presented in Figure 9. Seasonal outlier analysis using a Z-score threshold of $|Z| > 3$ further demonstrates the quality of the radiation measurements (Figures 10a–b). For SW radiation, only 0.152% of the observations were identified as outliers, with the highest seasonal occurrence during the monsoon season (JJAS), where outliers accounted for 0.126% of the measurements. Similarly, the LW radiation dataset exhibited an even lower outlier fraction of 0.075%, with the maximum seasonal occurrence observed during the pre-monsoon season (MAM) at 0.062%. All other seasons showed negligible outlier percentages, generally below 0.025%. Consequently, more than

99.848% of SW radiation observations and 99.925% of LW radiation observations were retained as valid measurements following quality-control screening. The exceptionally low outlier fractions and high data retention rates confirm the robustness of the quality-control procedures and the reliability of the long-term radiation observations acquired at the ARO.

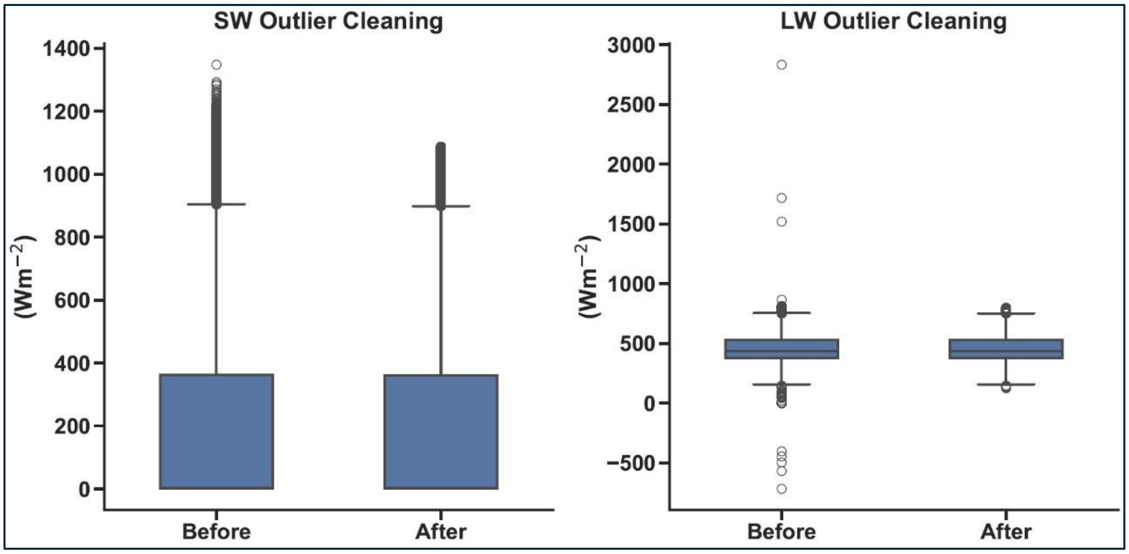

Figure 9: Box plot representation of radiation observations before and after quality-control

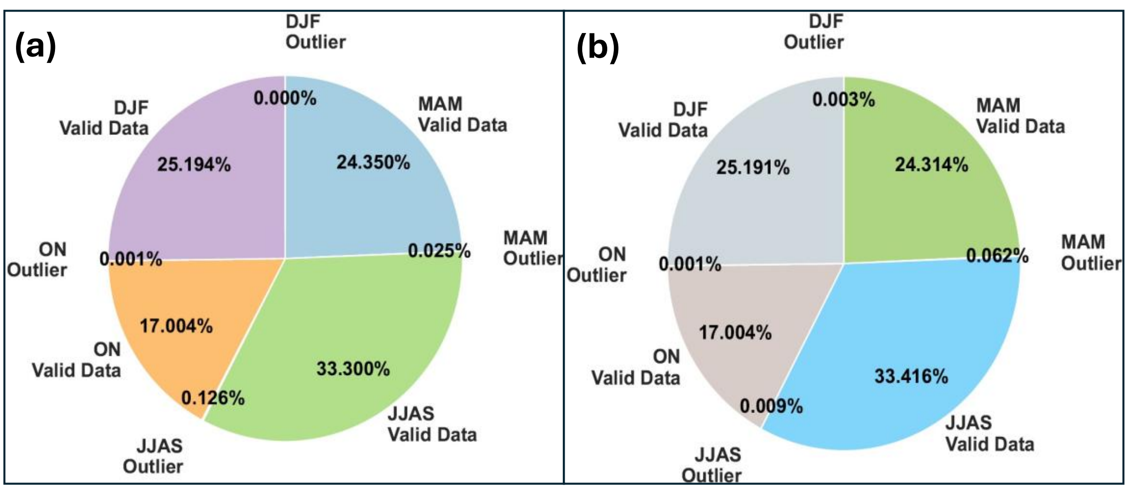

Figure 10. Seasonal distribution of valid and outliers identified using the Z-score method for (a) shortwave and (b) longwave radiation measurements.

7.3 Temporal consistency analysis

Temporal consistency analysis was conducted to assess the stability, continuity, and physical reliability of the measured shortwave (SW) and longwave (LW) radiation observations under different atmospheric conditions. Figures 11(a–b) show the temporal variability of SW and LW radiation under clear-sky conditions, while Figures 12(a–b) present the corresponding observations under cloudy-sky conditions.

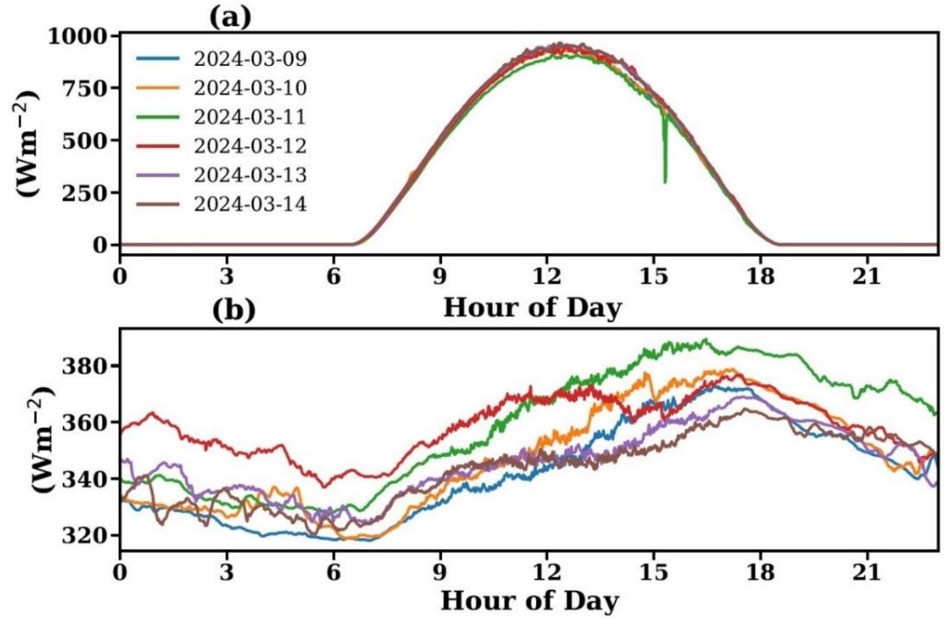

Figure 11: Temporal consistency analysis of (a) SW and (b) LW radiation under clear-sky conditions.

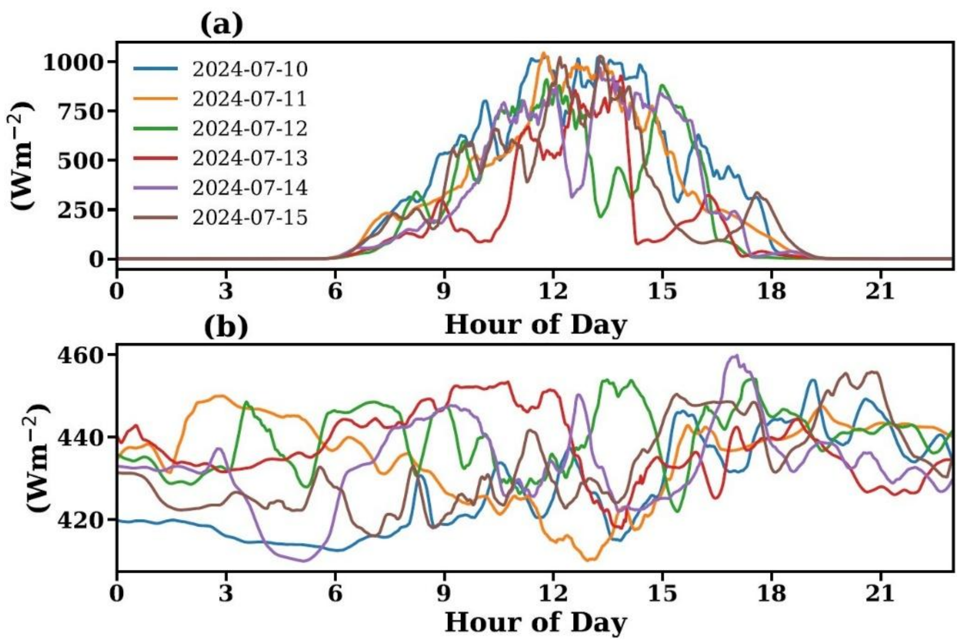

Figure 12: Temporal consistency analysis of (a) SW and (b) LW radiation under cloudy-sky conditions.

Under clear-sky conditions, SW radiation exhibits the expected smooth bell-shaped diurnal pattern, with values ranging from approximately 0 to 1000 W m^{-2} and peak irradiance occurring near local solar noon (Figure 11a). The corresponding LW radiation shows relatively smooth variations between 320 and 380 W m⁻² (Figure 11b). In contrast, cloudy-sky conditions produce substantial fluctuations in SW radiation due to cloud attenuation and scattering, resulting in values varying between 0 and 1000 W m⁻² throughout the day (Figure 12a). The associated LW radiation is enhanced under cloudy conditions, generally ranging from 410 to 460 W m⁻², owing to increased atmospheric emissivity and cloud longwave emission (Figure 12b). The observed temporal variations are physically consistent with expected radiative responses to changing atmospheric conditions and demonstrate the stability and reliability of the radiation measurements acquired at the observatory.

7.4 Clear-Sky model comparison

A clear-sky model comparison was performed by evaluating the observed SW radiation measurements against theoretical clear-sky irradiance estimates generated using the pvlib library (Holmgren et al., 2018) and the Ineichen clear-sky model (Ineichen and Perez, 2002) as illustrated in Figure 13. This assessment was undertaken to examine the physical consistency of the observations and to identify potential anomalies associated with sensor misalignment, shading effects, undetected cloud contamination, or instrumental uncertainties.

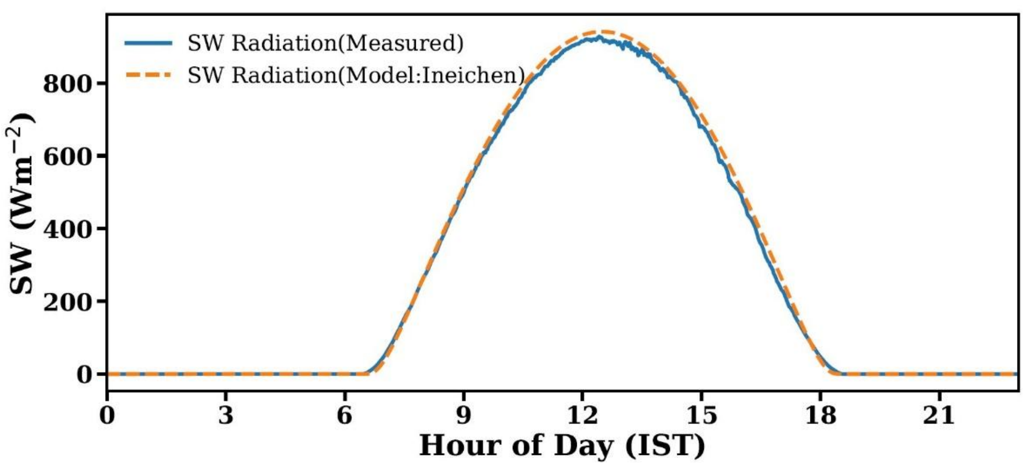

Figure 13: Comparison between observed and modelled SW radiation under clear-sky atmospheric conditions.

The comparison shows that the observed SW radiation closely follows the temporal evolution of the modelled clear-sky radiation, with excellent agreement in the timing of sunrise, solar noon, and sunset. The overall diurnal pattern and shape of the observed radiation curve are consistent with the theoretical clear-sky profile, indicating reliable sensor performance and accurate measurement of incoming solar radiation. However, the observed SW radiation magnitude is slightly lower than the modelled values throughout the daytime period. This difference is expected because the pvlib-based Ineichen model primarily utilizes site latitude, longitude, altitude, and solar geometry to estimate clear-sky irradiance and does not explicitly account for the actual atmospheric aerosol loading and aerosol optical depth (AOD) prevailing at the site. The presence of aerosols, water vapour, and other atmospheric constituents attenuates incoming solar radiation, resulting in lower observed irradiance relative to the idealized clear-sky estimates. Overall, the close agreement in diurnal timing and the physically consistent magnitude differences confirm the quality and reliability of the observed SW radiation measurements.

7.5 Instrument maintenance and recalibration logs

Regular instrument calibration and preventive maintenance activities are systematically documented and synchronized with the corresponding observational records. This practice helps identify periods affected by sensor recalibration, cleaning, component replacement, or operational adjustments, thereby accounting for sensor offsets, sensitivity variations, and performance changes during long-term data analysis. Such documentation improves the traceability, reliability, and scientific consistency of observational datasets.

8. Data Recovery and Gap-Filling Technique:

8.1 Interpolation methods

Interpolation methods are used to estimate short-duration missing radiation measurements and maintain the continuity of time-series datasets. When applied appropriately, these methods preserve data integrity and support subsequent quality-control procedures, statistical analyses, and modelling applications (Long and Shi., 2008; Driemel et al., 2018).

- Linear interpolation; is applied to very short data gaps (typically less than 5 minutes) where radiation variations are gradual and approximately linear over time.
- Spline interpolation; may be used for short missing intervals requiring smooth temporal reconstruction; however, its application is restricted to avoid introducing unrealistic fluctuations in rapidly varying radiation fields.

- Diurnal shape-preserving interpolation; utilizes the characteristic daily cycle of solar radiation to reconstruct missing observations under stable atmospheric conditions, particularly near the smooth radiation maximum around local solar noon.
- Large data gaps, periods affected by rapidly changing cloud conditions, and intervals exhibiting significant temporal variability are generally excluded from interpolation, as reconstruction under such conditions may introduce substantial uncertainties and reduce data reliability.

These interpolation procedures are intended to recover only a limited number of missing observations while preserving the physical consistency of the radiation measurements

8.2 Model-based reconstruction

Model-based reconstruction techniques are applied to estimate missing radiation measurements when direct interpolation is not suitable or when longer data gaps are encountered. These approaches utilize physically based and empirical relationships to improve dataset completeness while preserving the consistency of radiation measurements.

- For missing shortwave downward (SW↓) radiation data, clear-sky irradiance estimates generated using radiative transfer or pvlib-based clear-sky models are used as reference values and adjusted using nearby observations under comparable atmospheric conditions.
- For missing longwave downward (LW↓) radiation data, empirical parameterizations based on surface meteorological variables, such as air temperature, relative humidity, and cloud conditions employed where supporting observations are available.
- Statistical relationships between radiation components and ancillary meteorological parameters also utilized to reconstruct missing observations, provided that the derived relationships are physically consistent and adequately validated.

Model-based reconstruction is generally restricted to periods with sufficient supporting information and is not recommended for extended data gaps or rapidly changing atmospheric conditions, where reconstruction uncertainties may become significant. These methods help improve data completeness while maintaining the physical consistency required for long-term climate, energy balance, and atmospheric studies.

8.3 Machine learning-based imputation

Machine learning-based imputation techniques (Villegas-Mier et al., 2022; Costa et al., 2024) are applied to reconstruct longer data gaps (few hours to one day) and radiation measurements affected by complex atmospheric variability, particularly under cloudy conditions where conventional interpolation methods may be inadequate. Models such as k-Nearest Neighbour and Random Forest Regression are trained using historical radiation and meteorological observations to estimate missing values.

- Input features include time of day, day of year, and solar geometry parameters.
- Concurrent meteorological variables, such as air temperature, relative humidity, and atmospheric pressure, are incorporated to represent prevailing atmospheric conditions.
- Co-located or neighbouring sensor observations are utilized to improve reconstruction accuracy and maintain temporal consistency.

These approaches enhance data recovery for extended missing periods while preserving the temporal variability and physical characteristics of the radiation datasets.

9. Instrument Calibration

For calibration of radiation sensors, it must be removed and sent out for calibration to any center either in India or outside. This takes time and creates a long data gap. In order to maintain long-term measurement accuracy, stability, and radiometric traceability, periodic intercomparison is proposed and conducted between the operational radiation sensors (factory calibrated prior to deployment in field) and reference instruments (factory calibrated and maintained exclusively for periodic intercomparison, validation, and quality assurance activities) maintained at the observatory. The reference pyranometer is not operated continuously and is deployed only during selected routine intercomparison and validation periods to assess and verify the performance of the operational sensors. The intercomparison framework includes pyranometer, pyrgeometer, and PAR sensor. Simultaneous observations from the operational and reference instruments are evaluated.

The analysis focuses on identifying calibration drift, sensitivity variations, systematic bias, detector degradation, thermal-response effects, and alignment inconsistencies that may arise during long-term operation. The intercomparison was performed using six days of clear-sky observational data recorded simultaneously by both the reference instrument and the continuously operating field instrument under stable atmospheric conditions, as shown in Figure 14. Statistical parameters including the coefficient of determination (R^2), regression slope, intercept, percentage bias, and deviation from the 1:1 reference response were used to evaluate radiometric agreement, detector stability, and measurement consistency between the instruments.

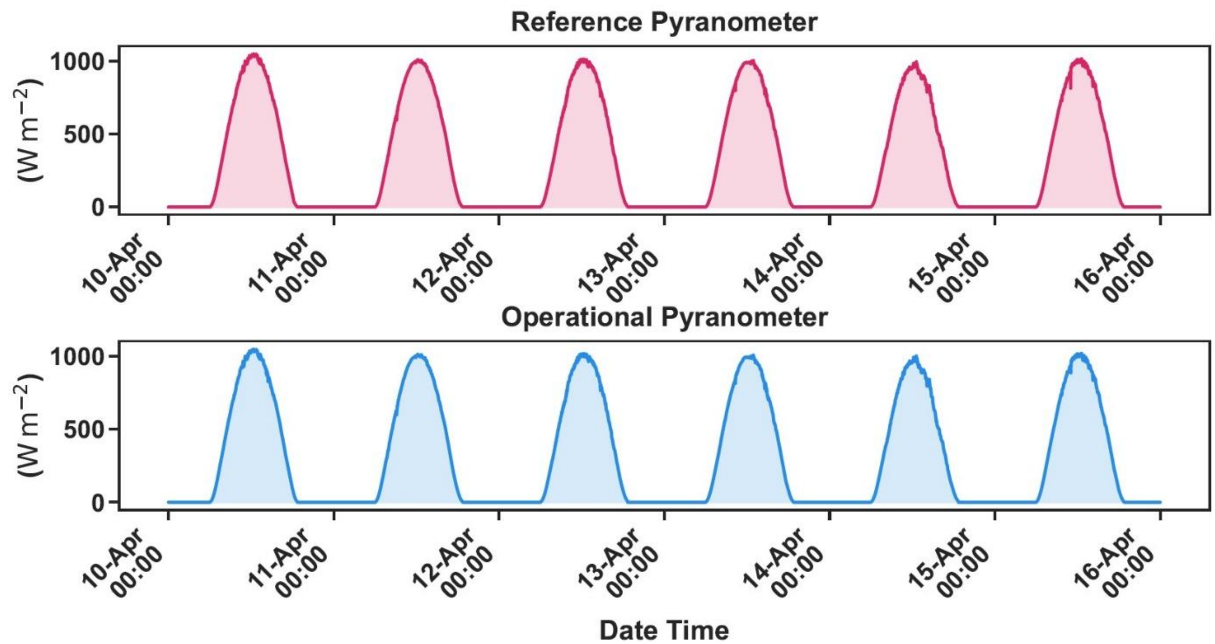

Figure 14: Inter-comparison of clear-sky SW radiation between reference and operational Pyranometers.

The intercomparison results provide an important quality-assurance framework for verifying observational reliability, supporting preventive maintenance, identifying recalibration requirements, and ensuring sustained high-quality radiation measurements for long-term atmospheric and climatological studies

9.1 Pyranometer (SW) Intercomparison Analysis:

The pyranometer intercomparison analysis demonstrates excellent agreement between the operational and reference instruments. The regression analysis yielded a very high coefficient of determination ($R^2 = 0.9998$), indicating an almost perfect linear relationship and highly consistent detector response across the analysed irradiance range. The regression slope of 1.0007 is extremely close to the ideal unity response, confirming negligible sensitivity drift and nearly identical radiometric responsivity relative to the reference instrument. The percentage bias of 0.81% further indicates minimal deviation between the two instruments. The close clustering of observations around the 1:1 reference line confirms excellent radiometric consistency with negligible systematic error, as shown in Figure 15(a). Overall, the operational pyranometer exhibits stable calibration characteristics and remains suitable for high-quality solar radiation monitoring applications.

9.2 Pyrgeometer (LW) Intercomparison Analysis:

The LW intercomparison analysis indicates acceptable agreement between the operational and reference pyrgeometers, with the instrument response remaining within acceptable observational uncertainty limits. The regression analysis yielded a coefficient of determination of ($R^2 = 0.9192$), indicating a reasonably strong linear relationship under varying atmospheric conditions. The regression slope of 0.992 is very close to the ideal unity response, indicating good radiometric agreement and stable sensor responsivity relative to the reference instrument, as shown in Figure 15(b). The percentage bias remains relatively small (0.632%), moderate observational scatter is observed across the analysed irradiance range. This variability is likely associated with dome-temperature effects, environmental thermal variability, and detector-response fluctuations commonly observed in LW radiation measurements.

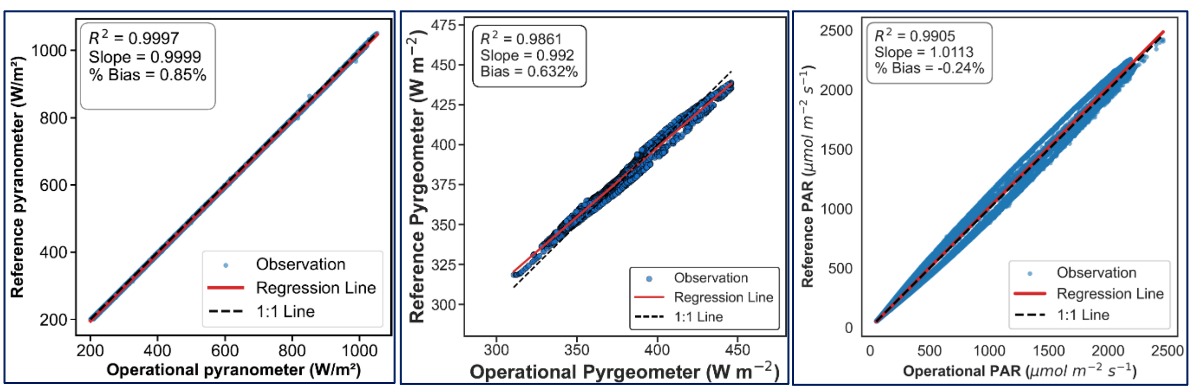

Figure 15: Performance analysis of pyranometer (SW), pyrgeometer (LW), and PAR sensor intercomparison

9.3 PAR Sensor Intercomparison Analysis

The PAR sensor intercomparison analysis indicates very good agreement between the operational and reference sensors, with a strong linear relationship observed throughout the analysed PAR range (R=0.9905). The regression slope of 1.0113 is very close to the ideal unity response, indicating minimal sensitivity variation relative to the reference sensor. The percentage bias of 0.24% remains very small, confirming stable detector response and measurement consistency.

Measurements remain closely distributed around the 1:1 reference line, indicating good radiometric consistency with minimal systematic deviation, as shown in Figure 15(c). The results confirm that the operational PAR sensor maintains stable calibration performance and is suitable for ecological, agricultural, and atmospheric radiation studies.

The intercomparison statistics obtained in this study are consistent with the performance characteristics commonly reported for research-grade radiometric observations. The high correlation coefficients, regression slopes close to unity, and low percentage bias values demonstrate stable detector response, good calibration consistency, and reliable long-term radiometric performance of the operational instruments.

The pyranometer intercomparison results ($R^2 = 0.9998$), regression slope (1.0007), and percentage bias (0.81%) indicate excellent agreement with the reference instrument and confirm high stability in SW radiation measurements. Similarly, the pyrgeometer observations ($R^2 = 0.9192$), slope (0.992), and percentage bias (0.632%) demonstrate acceptable radiometric consistency for LW radiation measurements, considering the inherent thermal-response variability and dome-temperature effects associated with atmospheric longwave observations. The PAR sensor statistics ($R^2 = 0.9905$), slope (1.0113), and percentage bias (0.24%) further indicate very good calibration stability and measurement consistency for photosynthetically active radiation observations. Overall, the intercomparison analysis confirms that the operational radiation sensors maintain acceptable radiometric accuracy, stability, and traceability for long-term atmospheric radiation monitoring.

10. Data Analysis

The observed radiation measurements demonstrate variability of SW, LW, UV, and PAR radiation parameters under different atmospheric conditions over the MCZ. Figures 16(a–b) show the radiation measurements obtained from the sun tracker, UV sensors, and PAR sensor under representative clear-sky and cloudy conditions, highlighting strong enhancement of GHI and DNI during clear skies and increased DHI under cloudy conditions due to enhanced cloud and aerosol scattering. Significant reductions in UV and PAR radiation are also observed during cloudy sky conditions because of increased atmospheric attenuation. Figures 17(a–b) present the corresponding variability of SW↓, SW↑, LW↓, and LW↑ radiation components measured by the net radiometer, demonstrating reduced incoming SW radiation and enhanced LW↓ radiation during cloudy and humid conditions associated with increased atmospheric emissivity and cloud water content.

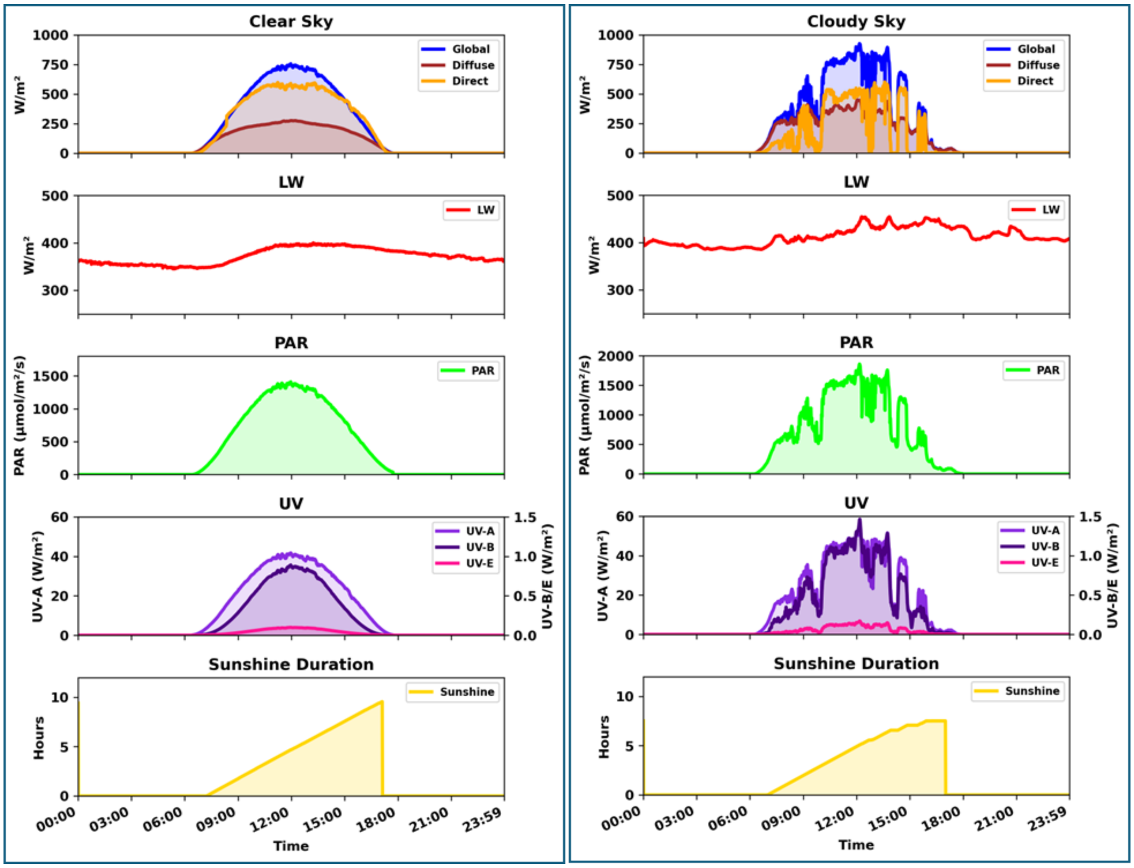

Figure 16: Different radiation parameters measured under clear-sky and cloudy sky condition

10.1 Clear-Sky Radiative Characteristics

Clear-sky conditions were characterized using periods with high SW radiation and low diffuse fraction ($DHI/GHI < 0.3$). Under these conditions, the radiation parameters exhibited smooth bell-shaped diurnal profiles closely following solar elevation. The mean clear-sky GHI was observed to be approximately 848 W m^{-2}, with peak values reaching ~1065 W m^{-2} during midday hours. Simultaneously, DNI remained the dominant SW component, with mean values around 762 W m^{-2} and peak values approaching 1001 W m^{-2}, indicating high atmospheric transmissivity and minimal cloud attenuation. Diffuse radiation remained comparatively low during clear-sky periods, with mean DHI around 193 W m^{-2}, confirming weak atmospheric scattering under cloud-free conditions. The lower diffuse fraction further demonstrates the dominance of direct-beam radiation during these periods. PAR exhibited strong enhancement under clear skies, with mean daytime values around 1587 μmol m⁻² s⁻¹ and peak values exceeding 2111 μmol m⁻² s⁻¹, indicating substantial photosynthetically active energy availability.

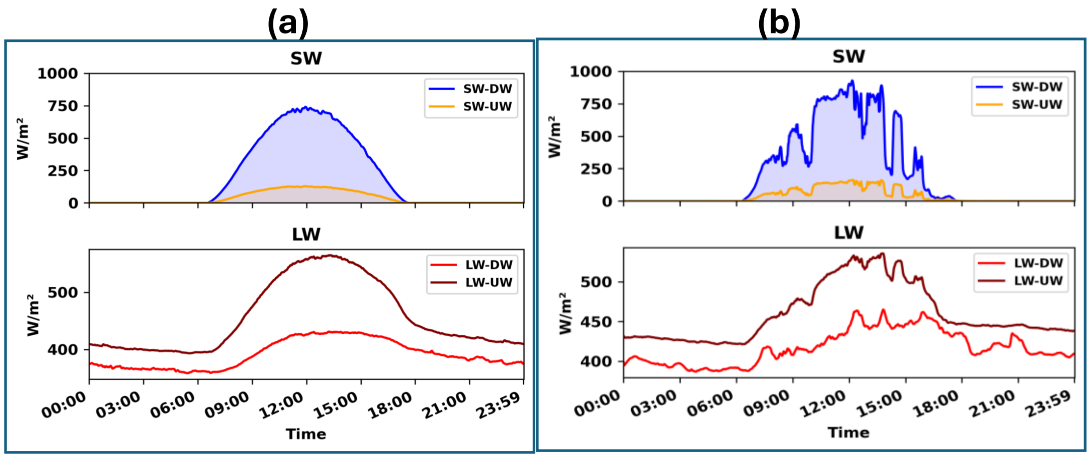

Figure 17: Radiation parameters measured by the net radiometer under (a) clear-sky and (b) cloudy conditions.

The UV radiation components also showed strong diurnal enhancement. Mean UV-A was approximately 45 W m⁻², while UV-B averaged around 1.2 W m⁻², with maximum values approaching 62 W m⁻² and 1.9 W m⁻², respectively. Under clear conditions, mean downward LW radiation remained comparatively lower at approximately 358 W m⁻², reflecting reduced atmospheric emissivity under relatively dry and cloud-free atmospheric conditions.

10.2 Cloudy and Overcast Radiative Characteristics

Cloudy conditions were identified using periods with dominant diffuse radiation ($DHI/GHI > 0.7$). Under these conditions, strong attenuation of direct solar radiation and enhanced diffuse scattering were observed. The mean GHI during cloudy periods reduced substantially to approximately 305 W m⁻², indicating significant suppression of incoming SW radiation by cloud systems. DNI experienced the strongest attenuation, with mean values decreasing to only 52 W m⁻², demonstrating nearly complete obstruction of direct solar beam radiation during dense cloud cover. In contrast, DHI became the dominant SW component during cloudy conditions, with mean values increasing to approximately 271 W m⁻² and peak values exceeding 698 W m⁻². This enhancement reflects intense multiple scattering by cloud droplets and atmospheric aerosols. PAR also decreased considerably under cloudy conditions, with mean daytime values reducing to approximately 641 μmol m⁻² s⁻¹. Similarly, UV-A and UV-B reduced to mean values of approximately 17 W m⁻² and 0.3 W m⁻², respectively, owing to strong cloud attenuation and atmospheric absorption. Unlike SW radiation, LW radiation exhibited substantial enhancement during cloudy conditions. Mean downward LW radiation increased to approximately 419 W m^{-2}, with peak values approaching 485 W m^{-2}, reflecting enhanced atmospheric emissivity associated with increased cloud water content and atmospheric moisture

10.3 Seasonal Diurnal Variation of SW and LW Radiation

The seasonal diurnal variation of SW and LW radiation exhibit distinct characteristics associated with changes in solar geometry, atmospheric thermodynamic conditions, cloud cover, and moisture availability across different seasons. The observed SW radiation shows a pronounced bell-shaped diurnal profile in all seasons, with maximum irradiance occurring near local solar noon. Among all seasons, the pre-monsoon period exhibits the highest mean peak SW radiation values, reaching nearly 900 Wm $^{-2}$, primarily due to clear-sky conditions, high solar elevation angles, low cloud cover, and enhanced incoming solar flux, as illustrated in Figure 18(a). In contrast, the monsoon season records the lowest mean peak SW radiation values, approximately 500 Wm $^{-2}$, mainly because of persistent cloud cover, increased atmospheric moisture, and enhanced scattering and absorption of solar radiation by clouds and aerosols.

During the post-monsoon season, mean peak SW radiation values increase to nearly 700 W m $^{-2}$ as cloudiness gradually decreases and atmospheric conditions become relatively clearer following the withdrawal of the monsoon. Winter exhibits comparatively lower mean peak SW radiation values of around 600 Wm $^{-2}$, mainly due to lower solar elevation angles, shorter daytime duration, and increased atmospheric attenuation associated with fog, haze, and winter aerosols. The smoother and more symmetric diurnal profiles observed during winter and pre-monsoon conditions indicate relatively stable atmospheric conditions, whereas the monsoon season shows larger short-term fluctuations associated with transient cloud passages and variable atmospheric instability, as evident from Figure 18(a). The seasonal variation of LW radiation also demonstrates clear dependence on atmospheric temperature, humidity, and cloud conditions. The highest mean LW radiation values are observed during the monsoon season, reaching nearly 430 Wm $^{-2}$, primarily due to enhanced atmospheric moisture content, higher cloud cover, and increased thermal emission from water vapour and clouds, as shown in Figure 18(b).

The pre-monsoon season records moderately high mean LW radiation values between approximately 380–400 Wm $^{-2}$, associated with elevated surface temperatures and warmer atmospheric conditions. During the post-monsoon period, LW radiation decreases to around 360–380 Wm $^{-2}$ as atmospheric moisture and cloud cover reduce progressively.

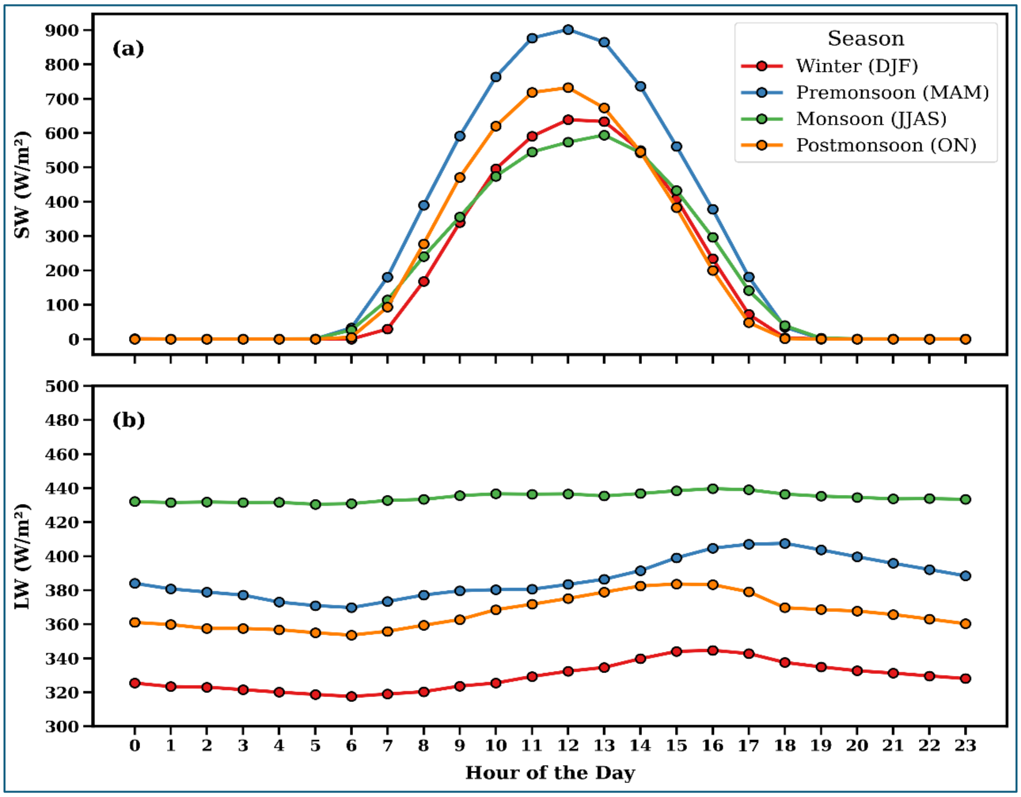

Figure 18: Seasonal diurnal variation of (a) SW and (b) LW radiation parameters.

The lowest mean LW radiation values are observed during winter, ranging between approximately 320–340 Wm $^{-2}$, mainly due to lower atmospheric temperatures, reduced water vapour content, and relatively weaker longwave emission from the atmosphere. The observed seasonal diurnal variation of SW and LW radiation clearly reflect the combined influence of solar geometry, cloud dynamics, atmospheric moisture, aerosol loading, and thermodynamic conditions over the study region. These radiation characteristics provide important insight into seasonal energy exchange processes and atmospheric radiative behaviour under tropical monsoon climatic conditions.

11. Future Vision:

The ARO established in monsoon core zone, central India will play a vital role in monsoon dynamics, atmospheric and climate research. The observations will advance radiative transfer studies, aerosol–cloud interactions, surface energy balance analysis, renewable energy forecasting, satellite and model validation. Future developments include upgradation of the facility, Artificial Intelligence and machine learning applications for automated quality control, cloud detection, aerosol characterization, and radiative forecasting by integrating surface, satellite, and numerical weather prediction data.

Acknowledgments: The authors thank the Director, IITM, for all the support and encouragement in establishing and maintaining ART facility in central India. The authors also acknowledge Prof. Ravi Nanjundiah and Dr. R. Krishnan, Ex-Directors IITM in establishing the ART facility in central India. Also acknowledge all the personal involved in installations and maintenance of the instruments and the facility.

Bibliography

1. Aeron. (2022). *XTREME Smart Data Logger Operational Manual* (Version IEC61400-12-1:2022). Retrieved from Aeron Systems XTREME Smart Data Logger
2. Augustine, J. A., DeLuisi, J. J., and Long, C. N. (2000). SURFRAD—A national surface radiation budget network for atmospheric research. *Bulletin of the American Meteorological Society*, 81(10), 2341–2357. https://doi.org/10.1175/1520-0477(2000)081<2341:SANSRB>2.3.CO;2
3. Bhat, G. S. (2006). The Indian drought of 2002 — A sub-seasonal phenomenon? Quarterly Journal of the Royal Meteorological Society, 132(621), 2583–2602. https://doi.org/10.1256/qj.05.13
4. Costa, T., Falcão, B., Mohamed, M.A. et al. Employing machine learning for advanced gap imputation in solar power generation databases. Sci Rep 14, 23801 (2024). https://doi.org/10.1038/s41598-024-74342-3
5. Dey, S., Tripathi, S. N., Singh, R. P., and Holben, B. N. (2004). Influence of dust storms on aerosol optical properties over the Indo-Gangetic basin. Journal of Geophysical Research, 109, D20211. https://doi.org/10.1029/2004JD004924
6. Driemel, A., Augustine, J., Behrens, K., et al. (2018). Baseline Surface Radiation Network (BSRN): structure and data description (1992–2017). *Earth System Science Data*, 10, 1491–1501. https://doi.org/10.5194/essd-10-1491-2018

7. Ga˘itan, N. C., Zagan, I., and Ga˘itan, V. G. (2024). Proposed Modbus extension protocol and real-time communication timing requirements for distributed embedded systems. *Technologies*, 12(10), 187. https://doi.org/10.3390/technologies12100187
8. Gadgil, S. (2003). The Indian monsoon and its variability. Annual Review of Earth and Planetary Sciences, 31, 429–467. https://doi.org/10.1146/annurev.earth.31.100901.141251
9. Gröbner, J., Emde, C., Wacker, S., et al. (2014). The new World Radiation Center facilities at Davos. *Geoscientific Instrumentation, Methods and Data Systems*, 3, 35–43. https://doi.org/10.5194/gi-3-35-2014
10. Haeffelin, M., et al. (2012). SIRTA, a ground-based atmospheric observatory for cloud and aerosol research. *Annales Geophysical*, 30, 1321–1340. https://doi.org/10.5194/angeo-30-1321-2012
11. Holmgren, W. F., Hansen, C. W., & Mikofski, M. A. (2018). pvlib python: A Python package for modeling solar energy systems. Journal of Open-Source Software, 3(29), 884. https://doi.org/10.21105/joss.00884 (Paper: https://joss.theoj.org/papers/10.21105/joss.00884)
12. Ineichen, P., & Perez, R. (2002). A new airmass independent formulation for the Linke turbidity coefficient. Solar Energy, 73(3), 151–157. https://doi.org/10.1016/S0038-092X(02)00045-2
13. Kazadzis, S., et al. (2018). Effects of aerosols and clouds on surface solar radiation. *Atmospheric Chemistry and Physics*, 18, 10077–10092. https://doi.org/10.5194/acp-18-10077-2018
14. Kipp and Zonen. (2018a). *SOLYS2 Sun Tracker Operational Manual* (Version A4-V1105). Retrieved from SOLYS2 Sun Tracker Manual
15. Kipp and Zonen. (2018b). *CGR4 and SGR4 Pyrgeometers Operational Manual* (Version v1811). Retrieved from CGR4 Pyrgeometer Manual
16. Kipp and Zonen. (2018c). *Pyrheliometer Operational Manual* (Version V1811-2). Retrieved from Pyrheliometers Manual
17. Kipp and Zonen. (2018d). *Sunshine Duration Sensors-CSD3 Operational Manual* (Version V1810). Retrieved from CSD3 Sunshine Duration Sensor
18. Kipp and Zonen. (2023a). *CMP Series Pyranometers Operational Manual* (Version v230719). Retrieved from CMP21 Pyranometer Manual
19. Kipp and Zonen. (2023b). *SUV Series Pyranometers Operational Manual* (Version v230525). Retrieved from SUV UV Radiometers Manual
20. Lau, K. M., Kim, M. K., and Kim, K. M. (2006). Asian summer monsoon anomalies induced by aerosol direct forcing: The role of the Tibetan Plateau. Climate Dynamics, 26, 855–864. https://doi.org/10.1007/s00382-006-0114-z
21. Le, L. H., Nguyen, D. T., Bui, H. P., Nguyen, C. C., and Ngo, T. Q. (2024). Integration of Modbus Ethernet communication for real-time electrical power consumption, temperature, and humidity

monitoring system. Preprint, Springer Nature, Research Square. https://doi.org/10.21203/rs.3.rs-4708973/v1

22. Long, C. N., and Shi, Y. (2008). An automated quality assessment and control algorithm for surface radiation measurements. *The Open Atmospheric Science Journal*, 2, 23–37. https://doi.org/10.2174/1874282300802010023
23. Moorthy, K. K., Satheesh, S. K., and Murthy, B. V. K. (2007). Investigations of marine aerosols over the tropical Indian Ocean. Journal of Geophysical Research, 112, D21201. https://doi.org/10.1029/2007JD008716
24. Padma Kumari, B., A. L. Londhe, S. Daniel, and D. B. Jadhav (2007), Observational evidence of solar dimming: Offsetting surface warming over India, Geophys. Res. Lett., 34, L21810, doi:10.1029/2007GL031133.
25. Padma Kumari, B., and B. N. Goswami (2010), Seminal role of clouds on solar dimming over the Indian monsoon region, Geophys. Res. Lett., 37, L06703, doi:10.1029/2009GL042133.
26. Sengupta, M., Habte, A., Gotseff, P., Weekley, A., and Lopez, A. (2015). Best practices handbook for the collection and use of solar resource data for solar energy applications. National Renewable Energy Laboratory (NREL). https://doi.org/10.2172/1225306
27. Villegas-Mier CG, Rodriguez-Resendiz J, Álvarez-Alvarado JM, Jiménez-Hernández H, Odry Á. Optimized Random Forest for Solar Radiation Prediction Using Sunshine Hours. Micromachines (Basel). 2022 Aug 27;13(9):1406. doi: 10.3390/mi13091406. PMID: 36144029; PMCID: PMC9505493.
28. Wild, M. (2012). Enlightening global dimming and brightening. *Bulletin of the American Meteorological Society*, 93(1), 27–37. https://doi.org/10.1175/BAMS-D-11-00074.1
29. Ying, S., Jin, H., Wu, X., Chunjie, J., Wei, G., and Ping, W. (2018). Research on Modbus bus protocol implementation technology based on single chip microcomputer. *2018 3rd International Conference on Information Systems Engineering (ICISE)*, Shanghai, China, 127–131. https://doi.org/10.1109/ICISE.2018.00031
30. Younes, S., Claywell, R., and Muneer, T. (2017). Quality control of solar radiation data: Present status and proposed new approaches. *Renewable and Sustainable Energy Reviews*, 73, 1228–1243. https://doi.org/10.1016/j.rser.2017.02.014
31. Zagan, I., and Ga˘itan, V. G. (2022). Enhancing the Modbus communication protocol to minimize acquisition times based on an STM32-embedded device. *Mathematics*, 10(24), 4686. https://doi.org/10.3390/math10244686

Annexure – I

Table 1: Key technical specifications of radiation sensors deployed at ARO

Sl. No.	Sensor	Model/Make	Specifications
1	Pyranometer	CMP21/Kipp & Zonen	Measures global and diffuse shortwave radiation: Spectral range: 285–2800 nm, sensitivity: 7 to 14 µV/W/m², response time: < 5 s.
2	Pyrheliometer	CHP1/Kipp & Zonen	For direct normal irradiance: spectral range: 200–4000 nm; sensitivity: 7 to 14 µV/W/m², response time: < 5 s.
3	Pyrgeometer	CGR4/Kipp & Zonen	Pyrgeometer for longwave radiation (outgoing and incoming); spectral range: 4500–42000 nm; 5 to 15 µV/W/m², response time: < 18 s.
4	UV-A	SFY/ Spectrafy	Measures UV-A irradiance (spectral range: 315–400 nm); suitable for outdoor solar radiation monitoring.
5	UV-B	SUV /Kipp & Zonen	Measures UV-B radiation (spectral range: 280–315 nm); response time: < 0.2 s, used for UV index and health exposure studies.
6	UV-E	SUV/Kipp & Zonen	Measures erythemal UV irradiance; response time: < 0.2 s, used for UV index, Output: 0–1 V analog.
7	Net Radiometer	CNR4 / Kipp & Zonen	Measures net radiation (shortwave: 300–2800 nm; longwave: 4500–42000 nm); integrates pyranometers and pyrgeometers.
8	PAR	Apogee	Measures extended photosynthetically active radiation (ePAR); spectral range: 400–750 nm; accurate for LED and sunlight.
9	Sunshine duration recorder	CSD3/Kipp & Zonen	Measures sunshine duration; provides digital output if direct radiation > 120 W/m²; spectral range: 400–1100 nm.
10	Sun Tracker	SOLIS2/Kipp & Zonen	A precision two-axis sun tracker designed for accurate alignment of direct solar radiation sensors; < 0.1° passive tracking / < 0.02° active tracking

*Note: A detailed technical description of each sensor is provided in Annexure II.

Annexure – II

Description of Radiation sensors

a. Pyranometer (CMP21)

The Pyranometer (Kipp and Zonen, 2023a) is a high-precision, research-grade instrument designed for continuous measurement of global solar irradiance on a horizontal plane, capturing both GHI & DHI solar radiation as shown in the Figure 19.1 (a). It is classified as a spectrally flat, class A sensor according to ISO 9060:2018, making it suitable for use in reference-grade solar radiation monitoring networks such as the WMO's BSRN (Driemel et al., 2018). The sensor operates across a spectral range of 285–2800 nm and provides a sensitivity of 7–14 µV/W/m², with a maximum solar irradiance capacity of 4000 W/m². It features a fast response time (< 5 s) and excellent thermal and directional stability, with zero offsets A and B below ±7 W/m² and ±2 W/m² respectively, and a directional error within ±10 W/m² for solar zenith angles up to 80°. The temperature response is within ±1% across an operational range of –40°C to +80°C.

The sensor is passively powered, outputting a low voltage signal proportional to incident radiation. A built-in thermistor provides temperature data for compensation. Each unit is individually characterized with calibration data for temperature and cosine response. Mechanically, the CMP21 includes a raised bubble level visible without removing the snap-on sun shield, a waterproof connector socket for signal cables, and a screw-in desiccant cartridge, making it robust for long-term field deployment (Kipp and Zonen, 2023a).

b. Pyrgeometer (CGR4)

The pyrgeometer (Kipp and Zonen, 2018b) (Figure 19.2 (b)) is a precision instrument designed for high-quality scientific measurements of longwave radiation emitted by the Earth's surface and atmosphere. The CGR4 operates over a spectral range of 4500 to 42000 nm, offering a sensitivity of 5 to 15 µV/W/m² and a response time of 18 seconds. It provides accurate measurements of net longwave irradiance in the range of -250 to +250 W/m², making it ideal for observing terrestrial radiation dynamics under varying atmospheric conditions. A unique feature of the CGR4 is its meniscus dome, which ensures a 180° field of view with negligible directional response error. The dome is externally coated with hard carbon, providing enhanced spectral smoothness and protecting the silicon surface. Its exceptional thermal stability eliminates the need for separate dome temperature correction or shading, improving measurement accuracy and simplifying deployment.

The CGR4 includes a waterproof socket compatible with Kipp & Zonen's signature yellow signal cable and features a snap-on sun shield that protects the bubble level and connector. The gold-plated connector allows for easy recalibration and maintenance. A screw-in drying cartridge ensures long-term stability by preventing internal condensation, with replacement desiccant readily available in refill packets. With its low window heating offset (< 4 W/m²), temperature dependence of sensitivity < 1%, and non-linearity < 1%, the CGR4 ensures high reliability in long-term environmental monitoring and atmospheric radiation studies across a broad operating temperature range of -40 to +80 °C (Wild, 2012).

c. **Pyrheliometer (CHP1)**

The pyrheliometer (Kipp and Zonen, 2018c) is a high-accuracy, research-grade radiometer designed for the precise measurement of DNI as shown in the Figure 19.1(c). Fully compliant with ISO 9060:2018 Spectrally Flat Class A standards, it is widely used in solar radiation monitoring networks and atmospheric research (Driemel et al., 2018). The instrument features a quartz window that transmits the full solar spectrum in the 200–4000 nm range. It offers a sensitivity of 7 to 14 µV/W/m², with a response time of less than 5 seconds, ensuring accurate and responsive measurements of direct solar radiation. Its narrow field of view (5 ±0.2°) and low non-linearity (< 0.2%) make it ideal for applications requiring high angular resolution, such as solar energy resource assessments and radiative transfer modelling (Sengupta et al., 2015).

To ensure thermal stability, the CHP1 is equipped with both a 10 kΩ thermistor and a Pt-100 temperature sensor, allowing for post-processing correction of temperature-dependent sensitivity variations using the provided calibration data. The instrument has excellent temperature performance, with a temperature dependency of sensitivity < 0.5% and an operational range of -40 to +80 °C. It also features a zero offset < 1 W/m² due to ambient temperature changes (5 K/h). The sensor is compatible with Kipp & Zonen SOLYS solar trackers, which are pre-fitted with mountings for CHP1, facilitating seamless integration in automated solar tracking systems (Kipp and Zonen, 2018a).

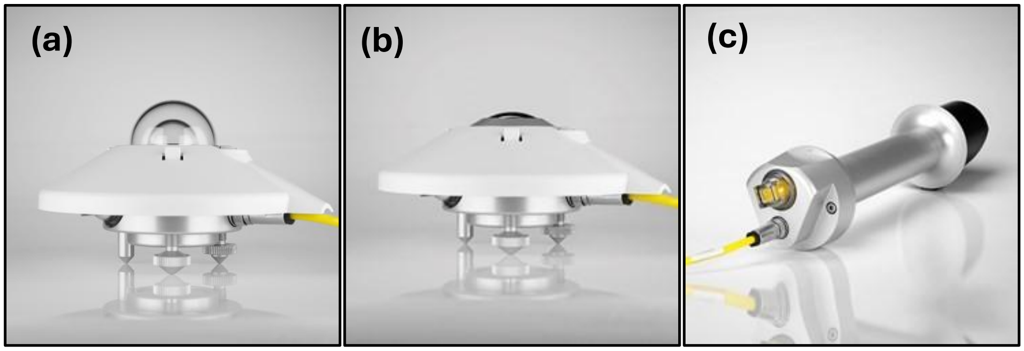

Figure 19.1: (a) Pyranometer (CMP21), (b) Pyrgeometer (CGR4), (c) Pyrheliometer (CHP1)

d. UV-A

The UV-A radiometer (Figure 19.2(a)) is a high-precision, multi-spectral radiometer designed for measurements of solar ultraviolet A radiation (UV-A) within the wavelength range of 315–400 nm as per ISO/CIE 17166 (Spectrafy). Utilizing filtered photodiodes and proprietary algorithms, the instrument performs direct spectral integration to resolve UV components, thereby avoiding common errors associated with traditional filter-based UV sensors. Its fast response time (<0.5 s), excellent cosine response (±3% at 80° zenith angle), and minimal temperature sensitivity (<0.1%) make it suitable for reliable field deployment. The UV-A also features integrated sensors for ambient temperature, atmospheric pressure, and relative humidity, supporting environmental monitoring and UV-dependent studies. With a calibration uncertainty of 1.1%, non-linearity and non-stability under 0.5%, and a maximum acquisition rate of 0.5 Hz, the instrument delivers robust performance for climate monitoring, public health UV forecasts, and agro-environmental research (Kazadzis et al., 2018).

e. UV-B

The UV-B radiometer is a precision instrument developed for the accurate outdoor measurement of ultraviolet B radiation within the wavelength range of 280 to 315 nm (Kipp and Zonen, 2023b). It is particularly suitable for environmental monitoring, atmospheric research, and health-related applications due to its high sensitivity and robust design as depicted in the Figure 19.2 (b). The sensor is equipped with an innovative quartz diffuser, which significantly improves its directional response, outperforming earlier models such as the CUV5 and SUV5. Additionally, its temperature correction mechanism is more accurate, ensuring consistent performance across varying environmental conditions. A precision glass dome, identical to that used in the CMP10 and CMP21 pyranometers, offers excellent protection for the internal optics, enhancing long-term stability and minimizing maintenance requirements. The SUV-B provides a 0 to 1 V analog output and supports Modbus RTU communication over a 2-wire RS-485 interface, enabling seamless integration with modern data logging systems (Zagan and Găitan, 2022; Găitan et al., 2024). The instrument operates on a 5V to 30V DC supply with a low power consumption of less than 55 mW, making it ideal for continuous remote deployments. Technically, it offers a response time of less than 0.2 seconds, non-linearity below ±1%, and a temperature response within ±1% across the operational range of −40°C to +70°C. Its directional response error is less than ±5% for solar zenith angles up to 70°, and it measures irradiance in the range of 0 to 9 W/m². UV-B radiation, although constituting only about 5% of the ultraviolet spectrum reaching the Earth's surface, has significant biological effects, including skin damage, sunburn, and DNA mutation. Therefore, precise monitoring is essential (Kazadzis et al., 2018). Each sensor is individually calibrated and provided with a detailed spectral response profile and correction matrices for solar zenith angle and total ozone column, allowing the user to achieve a measurement uncertainty of less than ±5% in daily UV-B totals after applying corrections (Kipp and Zonen, 2023b).

f. UV-E

The UV-E radiometer is a precision instrument optimized for measuring erythemal UV irradiance in accordance with the ISO/CIE 17166:2019 action spectrum, which reflects the human skin's sensitivity to sunburn shown in Figure 19.2(c) (Kipp and Zonen, 2023b). It enables direct calculation of the UV Index using the formula: UV Index = UVE (W/m²) × 40. The instrument features a quartz diffuser and dome for improved directional response and thermal stability. It provides a 0–1 V analog output and supports RS-485 Modbus RTU digital output, with a supply voltage of 5–30 V and power consumption below 55 mW (Zagan and Găitan, 2022; Găitan et al., 2024). Performance specifications include a spectral range defined by ISO/CIE 17166:2019, <0.2 s response time, <±1% non-linearity, <±1% temperature response over −40 to +70°C, and <±5% directional response up to a 70° solar zenith angle. The irradiance measurement range is 0 to 0.9 W/m². The SUV-E is supplied with individually measured spectral response data and correction matrices for zenith angle and ozone variation, ensuring typical measurement uncertainty of 5% (Kipp and Zonen, 2023b; Kazadzis et al., 2018).

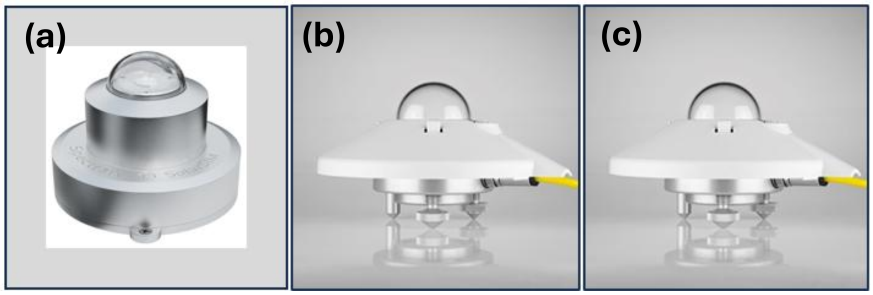

Figure 19.2: (a) UV-A (SFY) radiometer; (b) SUV-B radiometer; (c) SUV-E radiometer

g. Net Radiometer (CNR4)

The Net Radiometer is a precision instrument designed to measure the net radiation balance at the Earth's surface by quantifying both incoming and outgoing components of SW and LW radiation as illustrated in Figure 19.3 (a) (Wild, 2012; Kipp and Zonen, 2018b). It consists of two pairs of radiometric sensors: upward-facing and downward-facing pyranometers for short-wave radiation (300–2800 nm) and pyrgeometers for long-wave radiation (4500–42000 nm). All four sensors are integrated into a single compact housing, yet are individually calibrated to ensure high measurement accuracy. The upper long-wave sensor features a meniscus dome, offering an extended field of view (~180°) and effective water runoff, enhancing measurement stability under varying weather conditions.

Integrated within the body are two temperature sensors (Pt-100 and thermistor), used for thermal correction of infrared readings. These are positioned close to the long-wave detectors to ensure accurate compensation for housing temperature effects, thereby improving long-wave radiation accuracy. The lightweight design includes a built-in sun shield to mitigate thermal loading, and it uses waterproof yellow connectors common to all Kipp & Zonen radiometers. For environments where condensation, dew, or frost may affect measurements, the optional CNF4 ventilation and heating unit provides forced airflow and a heater (12 VDC, 1.25 A), which minimizes maintenance and ensures data continuity. The CNR4 offers a sensitivity range of 5–20 µV/W/m², response time under 18 s, non-linearity <1%, and operates reliably from –40°C to +80°C, making it suitable for continuous field deployment in diverse climatic conditions (Kipp and Zonen, 2018b; Driemel et al., 2018).

h. PAR

The PAR Sensor (Figure 19.3 (b)) is a precision quantum sensor designed to measure extended Photosynthetically Active Radiation (ePAR), covering the spectral range of 400 to 750 nm. Unlike traditional PAR sensors limited to 400–700 nm, the ePAR sensor captures additional far-red radiation (700–750 nm), which has been scientifically recognized for its role in enhancing photosynthesis and biomass accumulation, especially in dense canopies and under LED lighting environments. This makes the sensor particularly useful in modern plant science research, greenhouse monitoring, horticulture, and controlled environment agriculture (Sengupta et al., 2015).

The SQ-61x utilizes a silicon photodiode with a custom optical filter to ensure a spectral response that accurately replicates the extended PAR region. Housed in a rugged, weather-resistant anodized aluminium body, the sensor head is cosine-corrected to ensure accurate measurements across a wide range of solar zenith angles. The sensor supports various analog and digital outputs for easy integration with data loggers and environmental monitoring systems. Key performance characteristics include a measurement range of 0 to >4000 $\mu mol \cdot m^{-2} \cdot s^{-1}$, response time under 1 millisecond, and a cosine response accuracy within ±5% at 75° zenith angle. The sensor exhibits excellent stability with long-term drift under 2% per year and non-linearity under 1%. Operating temperature spans from –40°C to +70°C, and the sensor is suitable for continuous outdoor deployment or controlled environments. Each sensor is individually calibrated against a NIST-traceable reference under natural sunlight conditions. These features make the Apogee SQ-61x a reliable and scientifically robust solution for high-resolution ePAR monitoring across a wide range of plant and environmental research applications.

i. CSD3 Sunshine Duration Sensor

The Sunshine Duration Sensor (Kipp and Zonen, 2018d) is a high-precision instrument designed to measure sunshine duration in accordance with the WMO definition: the total time during which direct solar irradiance exceeds 120 W/m^2 as displayed in Figure 19.3 (c) (Driemel et al., 2018). Unlike traditional sunshine recorders that use mechanical or optical tracking systems, the CSD3 features no moving parts and instead utilizes three photodiodes with specially engineered diffusers to perform an analog determination of sunlight presence. Based on this, the instrument provides a digital high/low output indicating "sunny" or "not sunny" conditions, along with an analog output of the calculated direct irradiance.

The sensor has a spectral sensitivity range from 400 to 1100 nm, making it well-suited for broadband solar monitoring. It delivers a 1 ±0.1 V sunshine signal when direct solar radiation exceeds the 120 W/m^2 threshold, and the analog signal is proportional at 1 $mV/W/m^2$. The CSD3 achieves over 90% accuracy in measuring monthly sunshine hours and in detecting direct irradiance under clear-sky conditions. It boasts a rapid response time of under 1 millisecond, temperature stability of less than 0.1, and long-term non-stability of less than 2% per year. Designed for all-weather performance, the CSD3 includes built-in heaters to prevent the accumulation of rain, snow, or frost on the sensing elements. These heaters typically require 12 VDC power and are externally controlled, although an optional internal thermostat is available for autonomous operation. The sensor also features a humidity indicator and a large screw-type drying cartridge for easy maintenance. The robust construction, waterproof plug-and-socket connections, and extended operational temperature range of –40°C to +70°C make the CSD3 highly reliable for long-term, unattended outdoor deployments in diverse climatic conditions (Sengupta et al., 2015; Kipp and Zonen, 2018d).

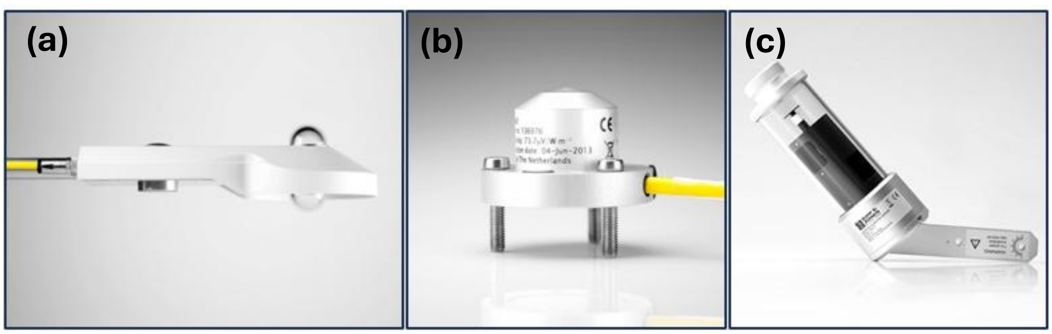

Figure 19.3: (a) CNR4 net radiometer; (b) PAR sensor and (c) CSD3 sunshine duration

j. SOLYS2 (Sun Tracker)

The Sun tracker (Kipp and Zonen, 2018a) is a high-precision, fully automated two-axis sun tracker widely used in solar energy and meteorological applications. Designed to meet BSRN performance standards, it offers superior pointing accuracy of <0.1° in passive mode and <0.02° with the optional active sun sensor as shown in Figure 19.4 (Driemel et al., 2018). The system features an integrated GPS receiver for automatic location and time configuration, eliminating the need for external computers or manual setup. Levelling is simplified with a built-in bubble level, while the rugged cast aluminium housing includes a tripod base with azimuth and zenith adjustment, ensuring stable and reliable alignment. SOLYS2 supports both 18–30 VDC and 100–240 VAC power supplies, with an internal heater extending its operating temperature range down to –40°C on AC power. It can accommodate a payload up to 20 kg, suitable for mounting multiple radiometers or pyrheliometers such as the CHP1. Optional top plates and shading assemblies allow complete solar monitoring station setups with up to three ventilated radiometers. Communication is facilitated via Ethernet and a web interface, while the drive mechanism uses durable inverted tooth belts. Power consumption is 21 W (reducing to 13 W at night), with an additional 100 W when the heater is active. The SOLYS2 combines robust performance, precision tracking, and ease of use, making it a leading choice in sun tracking instrumentation (Sengupta et al., 2015; Kipp and Zonen, 2018a).

Figure 19.4: SOLYS2 sun tracker

k. Aeron Data Logger

The observatory employs Aeron XTREME data logger as shown in Figure 19.5 to facilitate high-resolution acquisition of radiation parameters from a wide suite of sensors. Designed for research-grade performance, the XTREME series is equipped with a 24-bit high-resolution analog-to-digital converter (ADC), delivering over 20 Effective Number of Bits (ENOB), which ensures exceptional measurement precision (Aeron, 2022). The data logger supports sensor sampling rates up to 200 Hz, enabling high-fidelity, real-time data capture necessary for scientific investigations. To optimize data acquisition across the observatory, two Aeron XTREME loggers have been strategically deployed. One logger is exclusively dedicated to the CNR4 Net Radiometer. The second logger is configured to manage data from the Sun tracker, UV sensors, PAR and CSD3 sensors, thereby capturing dynamic variations in solar radiation data with fine temporal granularity. Each XTREME logger provides up to 8 differential or 16 single-ended input channels, accommodating a wide range of both analog and digital sensors. The system supports various measurement ranges, including 0–1 V, 0–5 V, 0–100 mV, and 4–20 mA, allowing flexibility in interfacing with diverse sensor types. The system maintains a measurement accuracy of ±0.03% Full Scale (FS) at 30°C, aided by a Delta-Sigma ADC architecture that enhances linearity and reduces noise. In addition, the XTREME loggers are engineered for low-power consumption and offer thermal stability, ensuring uninterrupted performance. Their continuous 24×7 operation ensures high-resolution data logging from all the sensors. The integration of these advanced data loggers enables automated, continuous, and reliable monitoring of the data. Their seamless interface with remote monitoring systems allows for real-time data access and analysis, thereby supporting both scientific research and operational decision-making (Le et al., 2024; Ying et al., 2018).

Figure 19.5: Aeron XTREME data logger.

The XTREME loggers are equipped with a versatile suite of communication interfaces, including Ethernet, Wi-Fi, and LTE, enabling both local and remote connectivity. This allows for real-time synchronization with centralized servers or cloud platforms, facilitating immediate access to streaming data from remote locations. The availability of serial communication protocols such as RS-232, RS-485, and SPI ensures compatibility with a wide array of digital and analog sensors, making the system adaptable (Le et al., 2024; Ying et al., 2018). To maintain the security and integrity of transmitted data, the loggers utilize encrypted communication protocols, including MQTT (Message Queuing Telemetry Transport) for lightweight messaging, HTTPS for secure web communication, and FTP for file transfers. These protocols safeguard the system against unauthorized access and ensure tamper-proof data delivery (Găitan et al., 2024; Zagan and Găitan, 2022). On the storage front, each XTREME logger includes a 32 GB external memory module, capable of handling extensive data volumes generated by high-frequency sampling. The system is designed to log up to 1000 parameters at 1-minute interval, supporting continuous data acquisition for up to three months without the need for data retrieval or manual intervention. For offline access and archival purposes, the system also supports USB connectivity, allowing users to extract large volumes of historical data quickly and conveniently. This functionality is particularly useful for field campaigns or during network downtime, providing redundancy and flexibility in data management (Aeron, 2022).